Journal of
Materials Chemistry A

Materials for energy and sustainability

Accepted Manuscript

This article can be cited before page numbers have been issued, to do this please use: A. Rau and K. Lu, *J. Mater. Chem. A*, 2025, DOI: 10.1039/D5TA03219A.

ROYAL SOCIETY OF CHEMISTRY

rsc.li/materials-a

View Article Online
DOI: 10.1039/D5TA03219A

Suppression of α-Quartz in Montmorillonite-SiOC Ceramic Nanocomposites with Water Vapor-Assisted Pyrolysis

Advaith V. Rau[a], Kathy Lu[a,b]*

[a]Department of Materials Science and Engineering, Virginia Polytechnic Institute and State University, Blacksburg, VA, 24061, USA

[b]Department of Mechanical and Materials Engineering, University of Alabama at Birmingham, Birmingham, AL, 35294, USA

*Corresponding author; Email: klu@uab.edu

Abstract

Bulk montmorillonite-silicon oxycarbide (MMT-SiOC) ceramic nanocomposites were fabricated with either Ar or Ar-H_2O pyrolytic atmospheres to determine the effect of water vapor on SiO_2 phase evolution at the MMT-SiOC interface and selectively etched porosity. While water vapor-assisted pyrolysis selectively removes free C in pure SiOC, surprisingly, MMT and water vapor in combination led to encapsulation, shielding, and retention of C as graphene oxide in MMT-SiOC-H_2O ceramics. Crystalline α-quartz phase in MMT-SiOC was converted to amorphous SiO_2 phase during water vapor-assisted pyrolysis, leading to 50-75% reductions in specific surface areas of HF-etched MMT-SiOC without changes to the intrinsic pore structure of water vapor-pyrolyzed SiOC. Further pyrolysis to 1400°C led to the dissolution of the aforementioned pore structure due to more extensive carbothermal reduction and refinement of β-SiC nanowhiskers. This work provides a new mechanistic understanding of how inorganic 2D

View Article Online
DOI: 10.1039/D5TA03219A

fillers (like MMT) can mediate chemical and structural evolution during polymer-derived ceramic synthesis.

Keywords: *silicon oxycarbide, montmorillonite, porous ceramics, silicon carbide, water vapor-assisted pyrolysis, ^{29}Si NMR*

1. Introduction

Silicon oxycarbide (SiOC) is a promising class of polymer-derived ceramics (PDCs) with notable thermal stability, oxidation resistance, and thermomechanical properties that offer attractive applications for aerospace, thermal insulation, catalyst supports, and lightweight structures. Classically amorphous, SiOC glasses are comprised of disordered SiO_xC_{4-x} ($1 \leq x \leq 3$) tetrahedra interspersed with SiO_2, SiC, and free carbon (C) regimes, in which the composition of Si-O-C tetrahedra may be tailored from the preceramic polymer(s) and pyrolytic temperatures and atmospheres.[1] Inert atmosphere pyrolysis between 800°C and 1100°C yields an amorphous SiOC matrix with SiO_2 amorphous domains and turbostratic C regimes spreading between SiOC clusters. Pyrolysis to 1300°C leads to β-SiC nucleation and growth from carbothermal reduction of amorphous SiO_2 and SiOC, although nuclei sizes are generally restricted to less than 5 nm.[2]

While containing an amorphous SiO_2 phase, SiOC glasses intrinsically exhibit low porosity after selective etching with HF as the SiO_2 phase is either sufficiently small (< 2 nm) or shielded by C and SiOC phases serving as diffusional and chemical barriers.[3] Porous SiOC is generally obtained through sacrificial additives to impart rationally controlled pore structures either through self-foaming during pyrolysis or selective etching of SiO_2. For PDC systems, sacrificial additives generally must be chemically compatible with preceramic polymers and the evolved ceramics, and

View Article Online
DOI: 10.1039/D5TA03219A

maintain coherency with the amorphous/nanostructured SiOC matrix in order to serve as reinforcements rather than inclusions. Promising sacrificial additives for PDCs are then reduced to polymeric fillers or novel oxide nanoparticles, which may require higher material or production costs.[4] Montmorillonite (MMT) clay additives are popular reinforcements in polymer nanocomposites as a low cost and sustainable filler from natural clay sources, leveraging the intrinsic two-dimensional (2D) nanostructured morphology of ~1 nm layered aluminosilicate sheets to improve mechanical properties and gas permeability, among others.[5] MMT additives are also attractive high-temperature reinforcements due to the inherent stability of the aluminosilicate sheet structure up to 1300-1400°C before phase separation to cristobalite and mullite.[6]

Novel MMT-SiOC ceramic nanocomposites were recently fabricated with twice-functionalized MMT nanoflakes to achieve an exfoliated 2D nanocomposite microstructure.[7] MMT nanoflakes were stabilized in the SiOC matrix through an interfacial α-quartz zone originating from the siliceous functional groups on the MMT surface. Selective etching of MMT-derived SiO_2 regimes indicated the emergence of small slit-like pores between 2 nm and 5 nm, but the relatively small specific surface areas (SSAs) of ~100 $m^2 \cdot g^{-1}$ for MMT-SiOC ceramics pyrolyzed to 1200°C in Ar elucidated that SiO_2 phase evolution from MMT was diffusion limited by excess free/turbostratic C present in MMT-SiOC ceramics. MMT nanoflakes are a promising material for introducing anisotropic pores owing to its 2D morphology but there is a need to improve the intrinsic porosity imbued by MMT structures and phase changes. Residual α-quartz also limits the viability of MMT-SiOC in elevated temperature applications due to the α-to-β quartz transition at ~573°C, during which the significant volumetric transformation can lead to fracture.

Reactive pyrolysis atmospheres (e.g., H_2O, H_2, CO) have been utilized to impart additional O, H, or C species and drive phase evolution in SiOC through radical-mediated reactions with Si

View Article Online
DOI: 10.1039/D5TA03219A

during the polymer-to-ceramic conversion between 400°C and 800°C.[8-14] Notably, water vapor-assisted pyrolysis has been shown to preferentially remove C as CO, suppress SiC formation, and accelerate SiO_2 crystallization in SiOC through an increase of Si-O-Si bonds and a decrease of Si-C bonds.[3,8,15,16] As excess C was evolved as CO gas in the presence of water vapor during the polymer-to-ceramic transition, any turbostratic C retained in the SiOC matrix was comprised of fewer graphitic layers, which diminished the barrier for atomic diffusion. C and O loss was detected by X-ray photoelectron spectroscopy (XPS) as the O_{1s}/Si_{2p} and C_{1s}/Si_{2p} peak ratios decreased from 3.997 and 0.625 in SiOC pyrolyzed at 1300°C in Ar to 3.433 and 0.294, respectively, in SiOC pyrolyzed with Ar + 16.7% H_2O, with H_2O injected between 500°C and 700°C.[3] These ceramics had compositions of $SiO_{1.24}C_{4.16}$ and $SiO_{1.77}C_{1.74,}$ respectively, as determined by elemental analysis that further confirmed that water vapor-assisted pyrolysis volatized C and minorly O.[3] H_2O-derived SiO_2 was susceptible to HF etching that produced highly porous SiOC with SSAs of ~2000 $m^2 \cdot g^{-1}$ and pore sizes between 2 and 5 nm for N_2 sorption experiments.[15] Pore distributions represented the 2-5 nm SiO_2 domains selectively-etched by HF, and N_2 sorption results agreed with transmission electron microscopy (TEM) imaging that revealed the size of both SiO_2 domains and mesopores.[3] Aided by C removal and OH introduction, soft ferromagnetic Ni-SiOC composites produced with water vapor-assisted pyrolysis to 900°C exhibited magnetic saturations up to 7.14 $emu \cdot g^{-1}$ and DC conductivities up to 247 $S \cdot m^{-1}$.[17] *In situ* metallic Ni and minorly NiO nanoparticles influenced these improvements from Ar+H_2O pyrolyzed SiOC (<1 $emu \cdot g^{-1}$, < 50 $S \cdot m^{-1}$),[17] which was noteworthy because $NiSi_y$ predominantly formed in carbon-rich SiOC pyrolyzed in Ar.[18] Water vapor-assisted pyrolysis is an attractive ceramic processing route to catalyze unique phase evolution mechanisms for novel multifunctional SiOC ceramics and composites.

View Article Online
DOI: 10.1039/D5TA03219A

H_2 pyrolysis atmospheres aggressively removed C to not only create visually "white" SiOC powders (compared to optically "black" SiOC from the high free/turbostratic C content) but also imbue photoluminescence from 410 nm to 530 nm with increasing pyrolysis temperatures from 800°C to 1100°C.[8,14,15] ^{29}Si nuclear magnetic spectroscopy (NMR) did not reveal substantial SiOC matrix composition changes after H_2 ingress as only the small concentration of $SiOC_3$ tetrahedra (<2-3%) inherently present in SiOC were removed by H_2, but ^{1}H NMR uncovered a higher concentration of C-H bonds and the emergence of Si-H bonds.[14] H_2-assisted pyrolysis was determined to primarily react with the free C phase through decarburization and H• implantation. In the presence of CO_2, Si-C and Si-N bonds were converted to Si-O bonds in SiOC and SiCN systems and reduced the Young's modulus and hardness by ~33%. CO_2 improved ceramic yields and decreased linear shrinkage during pyrolysis through the incorporation of O and was qualitatively evidenced with EDS depth profiles.[13,19] Free C evolved as CO *via* the Boudouard reaction, but these effects were limited to depths of 25-30 μm from the surface by limiting CO_2 exposure to less than 800°C.[13] CO_2-assisted pyrolysis is generally less investigated than either H_2- or H_2O-assisted pyrolysis and has not been appreciably reported for this material system apart from the aforementioned studies.

While reactive H_2 or CO_2 atmospheres were worthy of study, water vapor-assisted pyrolysis was chosen to deconvolute phase evolution mechanisms in MMT-SiOC that may be clouded during typical Ar pyrolysis or intrinsic to SiOC. By isolating the role of MMT in the context of the breadth of water vapor-assisted PDC research, this approach can be leveraged to other 2D nanomaterials such as MXenes (e.g., $Ti_3C_2T_x$), transition metal dichalcogenides (TMDs), layered double hydroxides (LDHs), or hexagonal boron nitride (h-BN) that have potential as supercapacitors, batteries, electrocatalysis, catalyst support, and piezoelectric energy harvesting,

View Article Online
DOI: 10.1039/D5TA03219A

among others. Inherently an oxide, MMT can be considered as a source for introducing templated porosity through SiO_2 domains derived with Ar+H_2O pyrolysis. This study focused on the effect of water vapor-assisted pyrolysis on SiO_2 phase formation in MMT-SiOC ceramics to evaluate the role of MMT nanosheet reinforcements as SiO_2 growth sites within the amorphous SiOC matrix (900-1200°C) and SiC nanowhisker growth at higher pyrolytic temperatures (>1400°C). Water vapor-assisted pyrolysis further served to selectively remove excess C during the polymer-to-ceramic transition, and the role of C as a diffusional barrier to SiO_2 phase growth was investigated. MMT content and pyrolytic processing temperature were varied to evaluate selectively etched porosity by N_2 sorption and microstructural features by X-ray diffraction, electron microscopy, and ^{29}Si NMR to understand phase evolution mechanisms and interfacial characteristics in MMT-SiOC ceramic nanocomposites.

2. Experimental methods

2.1. Materials

The materials for MMT exfoliation and functionalization were provided in a prior study.[7] A commercial polysiloxane (PSO, Polyramic SPR-684, [-Si(Ph)$_2$O-]$_3$[-Si(Me)(H)O-]$_2$[-Si(Me)(CH=CH$_2$)O-]$_2$, Starfire Systems, Inc., Glenville, NY) was the base preceramic polymer and cured with a 2.1% platinum-divinyltetramethyldisiloxane complex in xylene (Karstedt catalyst, Gelest, Inc., Morrisville, PA). Concentrated hydrofluoric acid (HF, 49 wt%, Avantor Specialty Materials, Inc., Radnor, PA) was used to selectively etch SiO_2 from the MMT-SiOC ceramics. Acetone (technical grade, Fisher Scientific, Waltham, MA), toluene (≥99.5%, Fisher Scientific, Waltham, MA), and ultrapure water (NP H_2O, 18.2 MΩ·cm) were used throughout the

View Article Online
DOI: 10.1039/D5TA03219A

experiment as general solvents. Argon (Ar, Industrial Grade, Airgas, Christiansburg, VA) was used for the pyrolysis atmosphere. All chemicals were used without further purification.

2.2. MMT-SiOC sample preparation and pyrolysis

AEAPTMS-functionalized MMT nanoflakes (AEAPMTS: (3-aminoethyl-2-aminopropy)trimethoxysilane) were synthesized from a naturally occurring clay source following a prior procedure.[7] *x*MMT-PSO preceramic green bodies (x = 0, 1, 2, 5 wt%) were prepared by mixing PSO with toluene (~50 v/v% relative to PSO), Karstedt catalyst (100 ppm relative to PSO), and functionalized MMT nanoflakes (100/0, 99/1, 98/2, 95/5 w/w). The suspension was stirred under vacuum to remove residual solvent. The polymer suspensions were cast to Φ12 mm x 6 mm cylindrical silicone molds, degassed under vacuum, and cured at 60°C for 6 h, 120°C for 6 h, and 150°C for 12 h. The green bodies were lightly ground and edges were slightly beveled to 1500 grit with SiC abrasive pads to remove any mold artifacts. To minimize potential surface oxidation, the green bodies were placed between two sheets of carbon felt in an alumina crucible.

The green bodies were pyrolyzed at 900°C, 1200°C, or 1400°C in a horizontal tube furnace (1830-12 Horizontal Tube Furnace, CM Furnaces, Inc., Bloomfield, NJ), with heating and cooling rates of 2°C·min^{-1}, soaking time of 2 h, and inflowing Ar of 500 cm^3·min^{-1}. Water vapor was injected between 500°C and 700°C by flowing Ar through a water bath maintained at 60±2°C (corresponding to 80 vol% Ar-20 vol% H_2O). The temperature was held for 30 min at 500°C and 700°C to ensure a thorough changeover of Ar to Ar-H_2O and Ar-H_2O to Ar, respectively. To mitigate batch-to-batch variations especially under reactive pyrolytic conditions, a typical furnace run consisted of at least 2 replicates of each *x*MMT-PSO (x = 0, 1, 2, 5) so a complete data set could be compared after each run; at least 3 furnace runs were conducted and samples with starkly

View Article Online
DOI: 10.1039/D5TA03219A

different trends in ceramic yields, sample shrinkage, and/or phase profiles from those reported previously and within this study were discarded.

MMT-SiOC ceramics prepared with water vapor-assisted pyrolysis were denoted as *x*MMT-T_{Pyr}-H_2O with x = 1, 2, 5 wt% and T_{Pyr} = 900, 1200, or 1400°C. Comparable MMT-SiOC ceramics were pyrolyzed without water vapor and denoted as *x*MMT-T_{Pyr}-Ar. Blank SiOC ceramics without MMT were similarly denoted SiOC-T_{Pyr}-Ar or SiOC-T_{Pyr}-H_2O.

2.3. Characterization

Ceramic yield and volume shrinkage were calculated from changes in mass and volume, respectively, between green bodies and pyrolyzed samples. Reported values were averages of 5-7 intact/unbroken replicates and corresponding errors indicated standard deviations. The phase compositions of powdered samples were analyzed with an X-ray diffractometer (XRD, Empyrean, Malvern PANalytical Ltd., Almelo, The Netherlands) operated at 40 kV and 40 mA with Cu Kα radiation between 2θ=3-90° and a scan rate of 0.02° s^{-1}. Microstructures were observed with a scanning electron microscope (SEM, JEOL IT-500HR, JEOL USA, Peabody, MA) and a transmission electron microscope (TEM, JEOL 2100, JEOL USA, Peabody, MA) with a LaB_6 filament operated at 200 kV. Simultaneous differential scanning and thermogravimetric analyses (STA, SDT 650, TA Instruments, New Castle, DE) were performed with a heating rate of 5°C min^{-1} to 1500°C under an argon flow of 20 mL·min^{-1}. Single-pulse magic angle spinning (MAS) nuclear magnetic resonance (NMR, Bruker Avance II, Bruker Corp., Billerica, MA) spectra for ^{29}Si were collected with a frequency of 59.627 MHz, 2.5 μs pulse width, 60 s recycle delay, averaged over 5000 scans, and in a 4 mm rotor at a MAS frequency of 10 kHz. ^{29}Si was calibrated by an external TMS standard (0 ppm). Raman characterization (XploRA PLUS, Horiba Scientific, Piscataway,

View Article Online
DOI: 10.1039/D5TA03219A

NJ) was performed with an Ar laser at 532 nm between 500-4000 cm^{-1}. Elemental analysis (E.A.) for Si (ICP-OES) and C (combustion) was performed by Galbraith Laboratories, Inc. (Knoxville, TN). Young's modulus and hardness were determined by nanoindentation (Nano Indenter G200, Keysight Technologies Inc., Santa Rosa, CA, USA) with a Berkovich diamond indenter to a peak displacement of 1 μm and averaged across a 5x5 array with 20 μm indent spacing. The samples were polished up to 0.1 μm with a diamond suspension prior to analysis. Porosity and surface area characteristics were determined by nitrogen adsorption at 77 K (Quantachrome Autosorb-iQ C-XR, Quantachrome Instruments, Boynton Beach, FL). Samples were degassed under vacuum at 300°C for 12 h before analysis. *x*MMT-SiOC ceramics were lightly fractured into ~5 mm pieces and etched in a 10% HF (aq) solution at 1 w/v% for at least 96 h. Samples were thoroughly washed with NP H_2O and EtOH and vacuum dried at 120°C for 12h. A Non-Local Density Functional Theory (NLDFT) model in the analysis software was applied to the adsorption branch with a spherical/cylindrical pore structure based on a silica adsorbate model to determine pore characteristics.

3. Results and discussion

3.1. Microstructural and phase evolution

As revealed in a preceding study,[7] exfoliated MMT-SiOC ceramic synthesis was heavily dependent on the MMT nanosheet synthesis and functionalization to not only imbue hydrophobicity and obtain single-to-few-layer nanoflakes, but also mitigate agglomeration or restacking effects between synthesis steps. Single-to-few-layer MMT nanoflakes were first obtained after freeze/thaw/sonication-assisted exfoliation and subsequently functionalized twice with cetriammonium bromide (CTAB) and AEAPTMS to impart a covalently-bound organophilic

View Article Online
DOI: 10.1039/D5TA03219A

silane coating. The previous study focused on phase and microstructural evolution in such novel MMT-SiOC nanocomposites, in particular noting that nanostructured MMT participated in SiOC-forming reactions during the polymer-to-ceramic transformation that was evidenced by interfacial α-quartz. This reactivity was leveraged in this study with water vapor-assisted pyrolysis to evaluate MMT as a source of templated porosity.

Phase compositions of MMT-SiOC ceramics pyrolyzed in Ar and Ar-20% H_2O were analyzed with XRD and shown in Figure 1. 1MMT-SiOC conditions were omitted due to similarities to 2MMT-SiOC conditions, and indexed reference patterns for identified crystalline phases were provided in the Supplementary Information. SiOCs pyrolyzed with Ar and Ar-20% H_2O were largely amorphous but with an increased amorphous SiO_2 (am-SiO_2) halo between 22-24° in both SiOC-900-H_2O (Figure 1(a)) and SiOC-1200-H_2O (Figure 1(b)) samples. While SiOC intrinsically yielded am-SiO_2 at 1400°C, SiO_2 formation was more pronounced in SiOC-1400-H_2O. All these observations are consistent with earlier studies,[3,8,15,16] indicating that water vapor pyrolysis accelerated SiO_2 formation and even SiO_2 crystallization in pure SiOC. However, in Figure 1(a-b), SiOC-900 and SiOC-900-H_2O samples, along with *x*MMT-900-Ar and *x*MMT-1200-Ar ceramics, exhibited crystallized α-quartz [trigonal; $P3_221$; PDF 00-033-1161] (100) and (101) reflections at 20.7° and 26.5°, respectively. We believe such α-quartz formation is transient in pure SiOC, as this phase disappeared in SiOC-1200 and SiOC-1200-H_2O (Figure 1(b)). These α-quartz peaks are absent for the SiOC-1200 and SiOC-1200-H_2O samples, likely due to the consumption of unresolved Si-OH bonds and α-quartz by conversion into SiOC through C

View Article Online
DOI: 10.1039/D5TA03219A

diffusion. am-SiO_2 and free turbostratic C phases likely reacted at higher pyrolysis temperatures, which was elucidated through recent ReaxFF/LAMMPS simulation studies.[20,21]

α-quartz crystallites were postulated to exist predominantly at the interface between MMT nanosheets and the SiOC matrix, as they are persistent in the xMMT-SiOC samples, also consistent with that reported previously.[7] With water vapor-assisted pyrolysis, however, α-quartz reflections were surprisingly less intense or fully suppressed in 1MMT-900-H_2O, 2MMT-900-H_2O, 1MMT-1200-H_2O, and 2MMT-1200-H_2O. The intensities of α-quartz reflections in 5MMT-900 and 5MMT-1200 were identical for both Ar and Ar-20% H_2O pyrolysis conditions, potentially due to bulk MMT effects from nanosheet coalescence at the high loading content. While all MMT-SiOC-H_2O samples pyrolyzed at 900°C and 1200°C exhibited a more pronounced am-SiO_2 halo, water vapor-assisted pyrolysis suppressed α-quartz crystallization at the MMT-SiOC interface. This opposed the general notion that water vapor-assisted pyrolysis facilitates SiO_2 formation. Fracture surfaces observed with SEM (Figure 2(a)) were identical among 2MMT-900 and 2MMT-1200 samples pyrolyzed with either Ar or Ar-20% H_2O, illustrating dense microstructures with faceted features in MMT-SiOC samples due to fracture at or along MMT domains. No discernible differences in SEM were expected due to similar MMT content across pyrolysis environments and changes to SiO_2 content occurring at the nanoscale. Suppressed α-quartz crystallization, however, indicated that water vapor-assisted pyrolysis may have reduced overall SiO_2 content and even SiO_2 domain size in MMT-SiOC, contradicting the typical behavior of SiOC with water vapor-assisted pyrolysis. SiOC-900-Ar and SiOC-900-H_2O as well as SiOC-1200-Ar and SiOC-1200-H_2O were similarly featureless, as expected.

Further pyrolysis to 1400°C (Figure 1(c)) corresponded to the increased presence of am-SiO_2 (~22-24° halo), turbostratic C [hexagonal; $P6_3/mmc$ (graphite); PDF 00-041-1487] (broad

View Article Online
DOI: 10.1039/D5TA03219A

(101) reflection at ~44°), and poorly crystallized β-SiC [cubic, $F\bar{4}3m$; PDF 04-002-9070] (broad reflections at 36°, 60°, and 72° for (111), (220), and (311) planes, respectively). While present in SiOC-1400-H_2O and 1/2/5MMT-1400-Ar, α-quartz was not observed in the XRD patterns of 2/5MMT-1400-H_2O, indicating that water vapor-assisted pyrolysis fully suppressed crystallization of the MMT-SiOC interface. The known increase in SiO_2 content in SiOC in the presence of water vapor seemingly contradicted the observed inhibition of α-quartz crystallization, alluding to the reduction of C as the driving mechanism. Free C in SiOC systems originated from excess C-rich functional groups in the preceramic polymer and existed as a continuous network that encapsulated SiO_2 regimes with the SiOC tetrahedra at the interlayer.[22] α-quartz was theorized to form upon cooling from high-temperature tridymite formed at the MMT-SiOC interface during the pyrolysis.

Identical emergence and strengthening of the 22° β-cristobalite [cubic, $Fd\bar{3}m$; PDF 04-007-2379] reflection among 2/5MMT-1400-Ar and 2/5MMT-1400-H_2O were attributed to MMT decomposition (an idealized form shown in Equation 2 in which M=Fe, Mg, Al depends on impurities in the clay composition), with the increasing reflection intensity correlating with the MMT content. In addition, β-SiC formation was enhanced in 2/5MMT-1400-H_2O as indicated by the increased prominence of (111), (200), and (311) reflections in Figure 1(c). MMT-SiOC pyrolyzed to 1400°C in Ar exhibited β-SiC nanowhisker growth (Figure 2(b-e)) from nanoflake MMT decomposition to cristobalite and mullite, of which the former formed β-SiC via carbothermal reduction with encapsulated and neighboring C regimes (Equation 1). β-SiC nanowhiskers were abundantly observed on *x*MMT-1400-Ar and *x*MMT-1400-H_2O fracture surfaces, randomly oriented and often protruding from the surface (Figure 2(b)). SiOC-1400-Ar and SiOC-1400-H_2O were similarly featureless and lacking β-SiC nanowhiskers, indicating that MMT addition primarily catalyzed nanowhisker growth (Figure 2(a)). The authors postulated that

View Article Online
DOI: 10.1039/D5TA03219A

nanowhisker growth was spurred by the small amount of mullite from MMT decomposition, because mullite exhibited needle-like morphologies in oxide ceramics[23-25] and *in situ* in a SiC composite.[26] XRD as a bulk technique could not detect mullite, not only because of the studied MMT concentrations less than 5 wt%, but also the small amount that would theoretically form due to its complex stoichiometry ($Al_6Si_2O_{13}$). However, as Al was detected by STEM-EDS in Figure 3, which will be discussed, mullite was expected to form while undetectable due to the presence of Al_2O_3 clusters within a very SiO_2-rich environment per the SiO_2-Al_2O_3 phase diagram.[27]

$$SiO_2 + 3C \rightarrow SiC(\beta) + 2CO\ (\uparrow) \quad (1)$$

$$Al_2M_2Si_4O_{10}(OH)_2 \Rightarrow SiO_2(\beta - Crs) + [3Al_2O_3 \cdot 2SiO_2](mullite) \quad (2)$$

However, these β-SiC nanowhiskers exhibited higher dendritic and non-steady state growth features (Figure 2(c-d)) compared to those present in MMT-SiOC-Ar.[7] The forked and coiled β-SiC nanowhiskers indicated that there was a general dearth of reactive C species, but this created a stark dichotomy with the XRD patterns showing enhanced β-SiC crystallization in MMT-1400-H_2O (Figure 1(c)). With water vapor-assisted pyrolysis, MMT-1400 ceramics formed more β-SiC, which required more C to be present as β-SiC formation proceeded purely through carbothermal reduction of SiO_2 in SiOC systems. Non-steady state growth observed at nanowhisker terminations was not attributed to the overall lack of reactive C, but to an insufficient amount relative to the higher concentration of β-SiC nanowhiskers formed near MMT flakes.

From these observations, we believed that MMT and water vapor-assisted pyrolysis in conjunction both suppressed SiO_2 crystallization and retained C in MMT-SiOC-H_2O, which was further observed and confirmed with (HR)TEM and STEM-EDS nanostructural characterization of 5MMT-1200-Ar and 5MMT-1200-H_2O (Figure 3). The MMT-SiOC interfacial region in 5MMT-1200-Ar (Figure 3(a)) was peppered with α-quartz nanoparticles in the generally

View Article Online
DOI: 10.1039/D5TA03219A

featureless SiOC matrix. Vein-like SiO_2 grains were observed to bridge the MMT-SiOC interface, which were further revealed (Figure 3(b)) to be comprised of both am-SiO_2 (white grains) and α-quartz (black particles). Crystalline α-quartz contributions were identified by minor diffraction spots in the FFT inset (yellow circles). MMT was shown previously to catalyze Si-O-Si condensation during pyrolysis of MMT-PSO around 400°C, a ~50°C earlier onset than in pure PSO, as the interfacial region between SiOC and MMT formed.[7] This interfacial region was theorized to comprise encapsulated C and SiOC clusters that bridged the coherency difference between crystalline MMT and am-SiO_2. α-quartz nanoparticles on the MMT surface (Figure 3(c)) and in the interface (Figure 3(d)) were well-crystallized with lattice fringes measured as 4.6 Å and 1.9 Å and attributed to (100) and (112) planes, respectively.

While 5MMT-1200-H_2O exhibited a similar morphology between MMT domains and the SiOC matrix (Figure 3(e)), the interfacial regions characterized by loss of crystallinity from α-quartz and encapsulated SiOC/C regimes were observed within or between MMT domains. The MMT-SiOC interfacial region (Figure 3(f)) exhibited solely am-SiO_2 grains with no crystalline α-quartz present. Water vapor injection suppressed α-quartz crystallization through amorphization of crystallized Si-O-Si bonds (Equation 3), which were shown to exhibit high reactivity with water in *ab initio* molecular dynamic simulations.[28] While high pressures have been shown to spur SiO_2 amorphization,[29,30] water vapor injection between 500°C and 700°C generated •H and •OH radicals that reacted with strained Si-O-Si bonds. Amorphization of Si-O-Si bonds further relieved lattice strain between crystalline regimes and the amorphous SiOC matrix. In the presence of MMT that created α-quartz prior to water injection, water vapor promoted am-SiO_2 formation through vitrification of crystalline α-quartz, accounting for the suppressed reflections observed in XRD (Figure 1).

View Article Online
DOI: 10.1039/D5TA03219A

$$R_3Si-O-SiR'_3\ (cr) + H_2O \rightarrow R_3Si-OH\ (am) + HO-SiR'_3\ (am) \qquad (3)$$

MMT regimes effectively shielded C from volatilizing as CO through encapsulation of SiOC/C regions during water vapor injection between 500°C and 700°C, as indicated in Figure 3(e). The lack of such encapsulated regions in 5MMT-1200-Ar indicated that water vapor not only promoted amorphization of Si-O-Si bonds but also C diffusion into SiO_2-rich regions. In this regard, water vapor may have led to additional SiOC clusters. HRTEM analysis within encapsulated regions (Figure 3(g)) revealed turbostratic C diffused between am-SiO_2 grains and characterized by a lattice fringe spacing of 4.4 Å corresponding to (002) C planes. The expanded interlayer spacing was due to C existing as graphene oxide, whose interlayer spacings are affected by O content and have been calculated by molecular dynamics simulations between 3.772 Å and 5.291 Å with increasing O group density from 10% to 50%.[31] Volatilization of C species (e.g., CH_4, $H_2C=CH_2$, $H_3C-CH_2=CH_2$) during Ar atmosphere pyrolysis is typical between 400°C and 700°C from excess C-rich functional groups in the preceramic polymer,[32-34] and water vapor-assisted pyrolysis further volatilizes free C as CO (Equation 4).[3,15] However, MMT domains shielded these encapsulated SiOC/C regimes from H_2O oxidation, and C was retained in the matrix. During typical Ar pyrolysis, ethylene and propylene primarily evolved between 500°C and 700°C as determined by TGA-MS (thermogravimetric analysis - mass spectroscopy) in related PDC systems.[32,33,35] This specific polysiloxane has not been analyzed with TGA-MS yet but closely resembled polycarbosilane (PCS) systems based on TG curves for PSO-to-SiOC[7] and PCS-to-SiC.[32,33] As water vapor was injected during this temperature range, radical-mediated reactions among Si, O, C, and H led to both C and O incorporation.[34] These reactions were summarized in Equations (5)-(7) in which amorphized Si-OH bonds reacted with volatilized hydrocarbons (X = H for ethylene and X = CH_3 for propylene).

View Article Online
DOI: 10.1039/D5TA03219A

$$C_{free} + H_2O \rightarrow CO\ (\uparrow) + H_2(\uparrow) \quad (4)$$

$$R_3Si - OH\ (am) \rightarrow R_3Si - O\cdot\ +\cdot H \quad (5)$$

$$CH_2 = C(H)X +\ \cdot H \rightarrow \cdot CH_2 - CH_2X \quad (6)$$

$$R_3Si - O\cdot + \cdot CH_2 - CH_2X \rightarrow R_3Si - O - CH_2 - CH_2X \quad (7)$$

EDS elemental maps of 5MMT-1200-Ar (Figure 3(i)) and 5MMT-1200-H_2O (Figure 3(j)) further revealed encapsulated SiOC/C regimes within MMT domains. MMT domains in both 5MMT-1200-Ar and 5MMT-1200-H_2O are Si ((Figure 3(i1)-(j1)) and O ((Figure 3(i2)-(j2)) rich, with C ((Figure 3(i3)-(j3)) generally segregated outside MMT domains. Al ((Figure 3(i4)-(j4)) and Fe ((Figure 3(i5)-(j5)) signatures were detected from the MMT nanosheet. However, as indicated in Figure 3(j4), C was detected within MMT regimes in 5MMT-1200-H_2O; this further confirmed that C was retained within MMT regimes and protected from water vapor ingress. Overall, water vapor-assisted pyrolysis produced inverse effects in MMT-SiOC ceramics as MMT domains preferentially retained C and water vapor induced α-quartz amorphization. Encapsulated SiOC/C regimes further enhanced β-SiC nanowhisker growth in MMT-1400-H_2O ceramics due to the carbothermal reduction of nanosized SiO_2 and C phases.

The elemental ratios in Table 1, taken in MMT domains and the surrounding SiOC, confirmed that MMT domains were SiO_2-rich compared to the C-rich SiOC matrix in both 5MMT-1200-Ar and 5MMT-1200-H_2O. With Ar+H_2O pyrolysis, Si (35.6 ± 1.2 at%) and O (28.2 ± 1.3 at%) contents increased within MMT domains at the expense of C (31.3 ± 1.7 at%) compared to Si (27.4 ± 1.5 at%), O (20.7 ± 0.4 at%), and C (47.8 ± 2.6 at%) concentrations in 5MMT-1200-Ar. Interestingly, Si (~12 at%), O (~16 at%), and C (~71 at%) ratios for the SiOC matrix were identical in both samples. While the SiOC matrix compositions were similar, the distribution of SiO_xC_{4-x} tetrahedra could differ but such information can only be ascertained with ^{29}Si NMR.

View Article Online
DOI: 10.1039/D5TA03219A

As previously mentioned, mullite was not observed in XRD or TEM owing to the marginal Al content (2-3 at%) within MMT domains in both samples. Fe was the primary substitutional atom within the nanosheet but was nearly negligible (<2 at%) in both samples; thus, in MMT-SiOC, Fe was not expected to substantially catalyze β-SiC formation as previously reported.[36-41] Encapsulated C regions in 5MMT-1200-H_2O exhibited a similar composition to the SiOC matrix and reinforced that MMT retained and encapsulated C as both free C and in SiOC during water vapor-assisted pyrolysis.

View Article Online
DOI: 10.1039/D5TA03219A

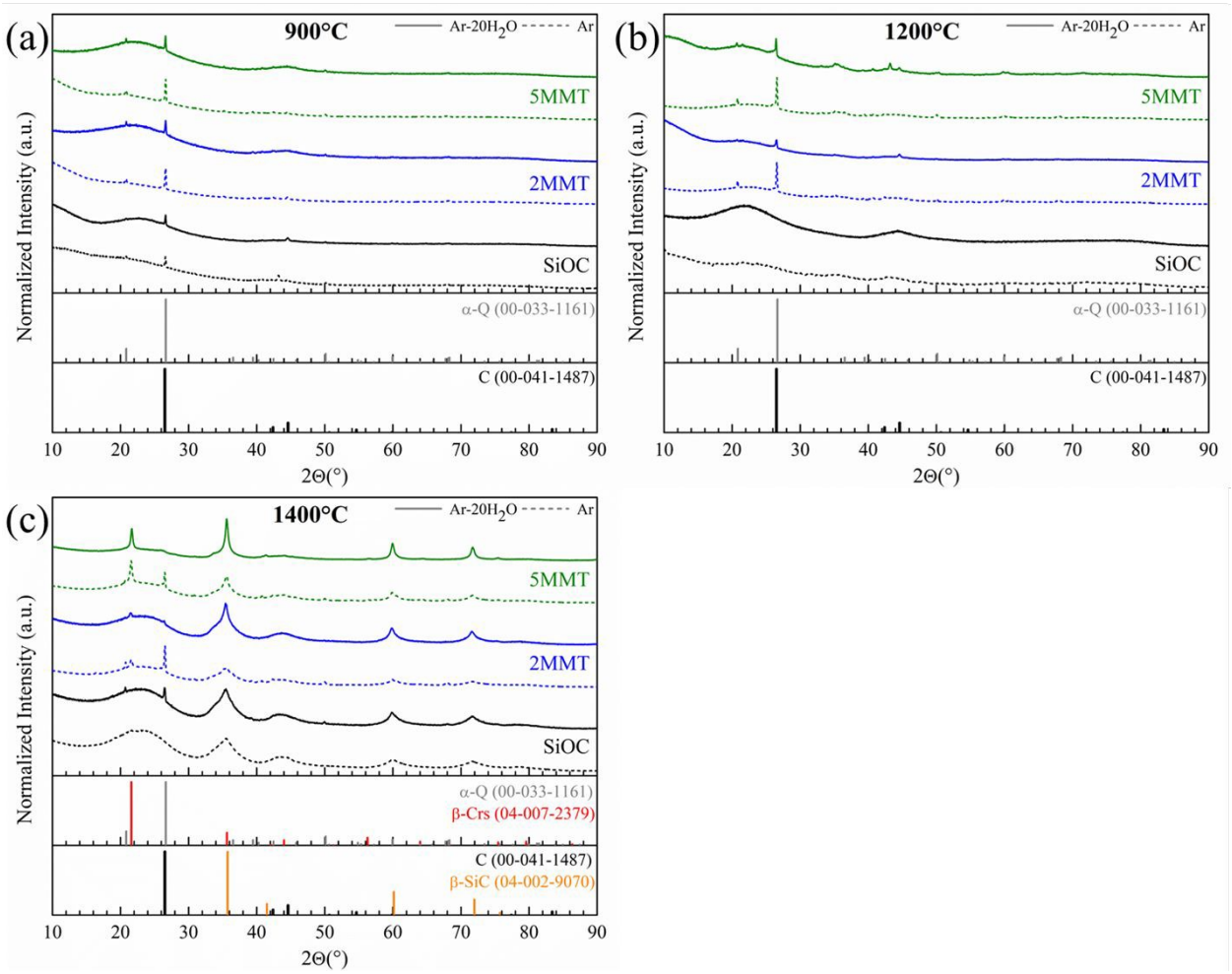

Figure 1. XRD patterns of *x*MMT-SiOC (*x* = 0, 2, 5) ceramics pyrolyzed at (a) 900°C, (b) 1200°C, and (c) 1400°C in Ar-20%H_2O (solid) and Ar (dotted). XRD patterns for 1MMT-SiOC were similar to 2MMT-SiOC at all temperatures and were omitted for brevity. The curves were normalized and offset for clarity, and the reference XRD patterns for α-quartz (α-Q; 00-033-1161), β-cristobalite (β-Crs; 04-007-2379), β-SiC (04-002-9070), graphitic carbon (C; 00-041-1487) were provided from ICDD PDF cards.

View Article Online
DOI: 10.1039/D5TA03219A

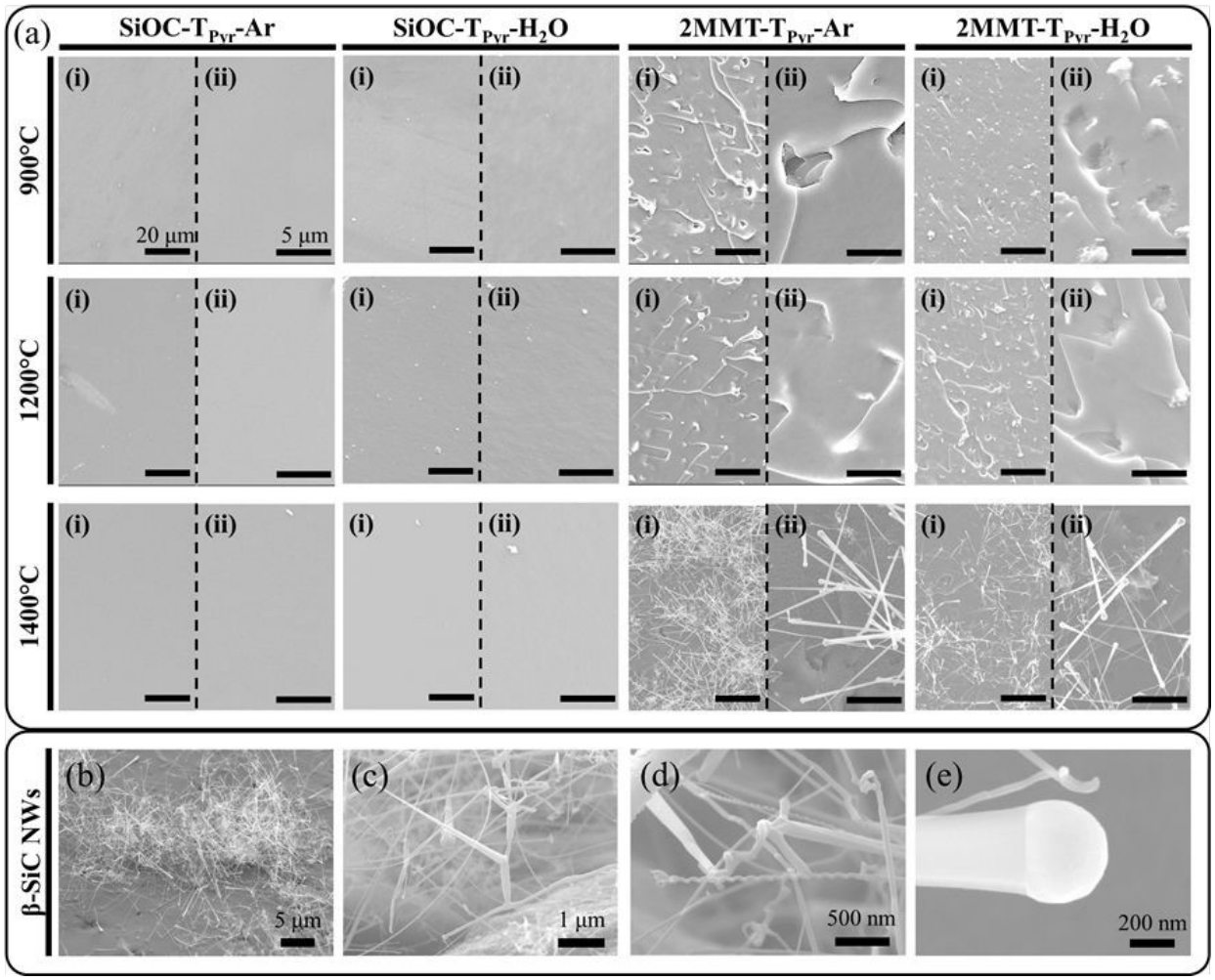

Figure 2. (a) Fracture surface morphologies of SiOC and 2MMT-SiOC ceramics pyrolyzed to 900°C, 1200°C, and 1400°C with Ar or Ar-20% H_2O. Scale bars in panels (i) and (ii) in all micrographs are 20 and 5 µm, respectively; (b)-(d) β-SiC nanowhisker structures formed during water vapor-assisted pyrolysis of 1/2/5MMT-SiOC to 1400°C, illustrating a non-steady state and dendritic growth; (e) detached SiO_2 nodule from which β-SiC nanowhiskers form.

View Article Online
DOI: 10.1039/D5TA03219A

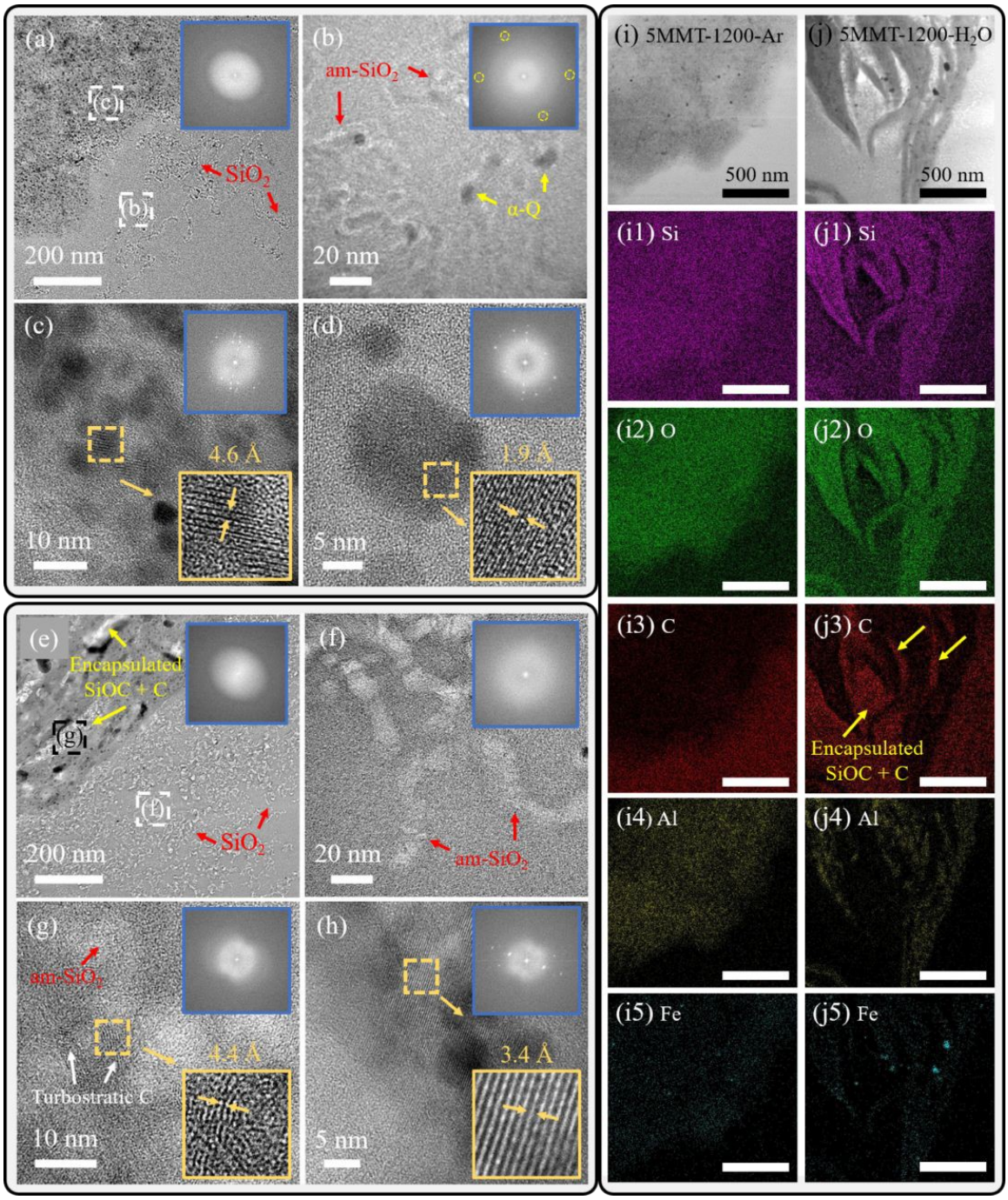

Figure 3. (HR)TEM characterization of (a)-(d) 5MMT-1200-Ar and (e)-(h) 5MMT-1200-H_2O cross-sections prepared by FIB lift-out. Blue-outlined insets show respective FFT patterns and orange-outlined insets show enhanced views of lattice fringes. STEM-EDS elemental maps for Si

View Article Online
DOI: 10.1039/D5TA03219A

(1/purple), O (2/green), C (3/red), Al (4/yellow), and Fe (5/blue) of (i) 5MMT-1200-Ar and (j) 5MMT-1200-H_2O. Scale bars in all (i)/(j) panels are 200 nm.

Table 1. Elemental ratios from STEM-EDS of Si, O, C, Al, and Fe in 5MMT-1200-Ar and 5MMT-1200-H_2O. Values represented the averages and standard deviations of 3 different regions within each location: MMT domains (MMT), SiOC matrix (SiOC), and encapsulated C regions in 5MMT-1200-H_2O (Encaps. C). n.d. – not determined. The EDS spectra are provided in the Supplement Information (Figure S-5).

Sample	**Location**	**Elemental Composition (at%)**				
		Si	O	C	Al	Fe
5MMT-1200-Ar	MMT	27.4 ± 1.5	20.7 ± 0.4	47.8 ± 2.6	2.5 ± 0.5	1.6 ± 0.2
	Matrix	12.1 ± 0.4	16.4 ± 0.1	71.5 ± 0.3	n.d.	n.d.
5MMT-1200-H_2O	MMT	35.6 ± 1.2	28.2 ± 1.3	31.3 ± 1.7	3.6 ± 0.1	0.6 ± 0.3
	Matrix	12.4 ± 0.5	16.2 ± 0.1	71.3± 0.5	n.d.	n.d.
	Encaps. C	15.5 ± 5.0	18.4 ± 2.0	65.4 ± 7.0	0.5 ± 0.1	0.2 ± 0.1

3.2. Physical and mechanical properties

Water vapor-assisted pyrolysis produced MMT-SiOC-H_2O ceramics that showed a higher retention of C, which had further implications in overall physical properties. Figure 4 summarizes the ceramic yield (CY, top panel/black) and volumetric shrinkage (VS, bottom panel/blue) of MMT-SiOC-Ar and MMT-SiOC-H_2O pyrolyzed at (a) 900°C, (b) 1200°C, and (c) 1400°C. Ceramic residues of MMT-SiOC-H_2O samples pyrolyzed at 900°C were 3-5% greater than corresponding MMT-SiOC-Ar ceramic yields. The ceramic yields of 1/2/5MMT-900-Ar (CYs: ~77.7 ± 0.8%) were not discernible from those of SiOC-900-Ar (CY: 77.0 ± 0.8%) within experimental error. While water vapor-assisted pyrolysis improved the ceramic yield between SiOC-900-Ar and SiOC-900-H_2O (CY: 82.0 ± 0.2%) by 5%, 1/2MMT-900-H_2O (CYs: ~80.5 ±

View Article Online
DOI: 10.1039/D5TA03219A

0.3%) and 5MMT-900-H_2O (CY: 81.7± 0.5%) ceramics only showed a 3% improvement compared to 1/2/5MMT-900-Ar. Presumably, MMT inhibited expected reactions between water vapor and the transforming MMT-PSO/MMT-SiOC matrix, hence limiting C removal or OH incorporation caused by water vapor pyrolysis. The observed higher CYs between 2MMT-900-H_2O and 5MMT-900-H_2O were attributed to the bulk MMT effects from coalesced MMT regimes.

In addition, water vapor-assisted pyrolysis did not affect volumetric shrinkage (Figure 4(a)) among SiOC-900-Ar (VS: 39.9 ± 0.6%), SiOC-900-H_2O (VS: 40.9 ± 0.3%), 1MMT-900-Ar (VS: 39.4 ± 0.7%), and 1MMT-900-H_2O (VS: 40.0 ± 0.4%). While causing an additional ~2% shrinkage difference between 2MMT-900-H_2O (VS: 41.6 ± 0.4%) and 2MMT-900-Ar (VS: 39.2 ± 0.9%), water vapor-assisted pyrolysis accentuated the expected bulk MMT effects at 5% MMT loading with a ~4% difference between 5MMT-900-H_2O (VS: 42.3 ± 0.2%) and 5MMT-900-Ar (VS: 38.4 ± 0.7%). Even though it induced notable changes to the pure SiOC matrix, water vapor pyrolysis was not sensitive to increasing MMT content up to 2% as the trends between SiOC-900, 1MMT-900, and 2MMT-900 were identical regardless of pyrolysis atmosphere. Therefore, water vapor pyrolysis of MMT-SiOC affected SiO_2 phase formation both in the SiOC matrix and in MMT domains, but with inverted effects.

Further pyrolysis to 1200°C generally contributed to ~1.5-2% greater ceramic yields (Figure 4(b)) in SiOC-1200-H_2O (CY: 74.5 ± 0.5%) and 1/2/5MMT-1200-H_2O (CY: ~76.9 ± 0.6%) than for Ar-pyrolyzed SiOC-1200 (CY: 73.5 ± 0.3%) and 1/2/5MMT-1200 (CY: ~75.5 ± 0.5%), which were expected from oxygen/hydroxyl incorporation during water vapor-assisted pyrolysis. Ceramic yields among 1/2/5MMT-1200-H_2O and 1/2/5MMT-1200-Ar were nearly identical and not discernible within experimental error. As shown in Figure 3(b), the net mass

View Article Online
DOI: 10.1039/D5TA03219A

increase corresponded with a general ~2.5-3% lower volumetric shrinkage across SiOC-1200 and 1/2/5MMT-1200 pyrolyzed with Ar-20%H_2O compared to the Ar-pyrolyzed analogs.

Volumetric shrinkage in MMT-SiOC-1200 samples was primarily caused by matrix reactions with the water vapor pyrolysis environment: shrinkage increased to 48.3 ± 0.6% in SiOC-1200-H_2O from 45.2 ± 0.6% in SiOC-1200-Ar. No significant differences were observed in 1MMT-1200-H_2O (VS: 48.1 ± 0.8%) and 1MMT-1200-Ar (VS: 45.3 ± 0.4%) compared to the corresponding SiOC-1200 samples, as 2 wt% MMT was ostensibly the critical loading concentration. The samples with MMT content above 2% exhibited slight VS decreases of ~1-1.5% across either pyrolysis atmosphere, with 2MMT-1200-H_2O (VS: 43.8 ± 0.8%) vs. 2MMT-1200-Ar (VS: 47.3 ± 0.8%) and 5MMT-1200-H_2O (VS: 44.7 ± 0.6%) vs. 5MMT-1200-Ar (VS: 46.3 ± 0.5%), continuing the aforementioned trend between Ar-20% H_2O and Ar pyrolysis atmospheres. Notably, the increase in ceramic yield among *x*MMT-1200-H_2O was associated with the absence or suppression of α-quartz phases (Figure 1(b)). This indicated that water vapor-assisted pyrolysis of MMT-SiOC did not appreciably introduce SiO_2 around the MMT-SiOC interface but rather predominantly occurred in the SiOC matrix, as suggested earlier. The associated mass gain was believed to originate from retained SiOC or C around the interface that was either resistant to reactions or was introduced *via* water vapor-assisted pyrolysis.

CYs of Ar-pyrolyzed MMT-SiOC decreased by 2-5% between 900°C and 1200°C primarily due to H_2 evolution from resolved Si-OH bonds. Transient α-quartz in SiOC-900 disappeared in SiOC-1200 for both Ar- and water vapor-pyrolyzed ceramics, indicating that 1200°C pyrolysis was required to achieve a complete SiOC matrix without lingering -OH moieties. This effect was more noticeable in water vapor-pyrolyzed MMT-SiOC with a generally larger CY decrease of 4-8% between 900°C and 1200°C because H_2O injection contributed more -OH and -

View Article Online
DOI: 10.1039/D5TA03219A

H groups in the SiOC matrix. While present in 2MMT-900-H_2O, residual α-quartz was indiscernible in 2MMT-1200-H_2O and similarly resolved into am-SiO_2 as in native SiOC. α-quartz in 5MMT-1200-H_2O was caused by agglomeration and was inaccessible to H_2O ingress, while α-quartz in 2/5MMT-1200-Ar was not reactive with the transforming SiOC matrix between 900°C and 1200°C.

The reduction of residual α-quartz between 900°C and 1200°C suggested MMT-SiOC interface refinement as H_2 was released and lingering interfacial Si-OH formed Si-O-Si or Si-O-C bonds. Elastic modulus (E) and hardness (H) values determined by nanoindentation (the indentation curves are in the Supplement Information Figure S-4) surprisingly revealed differing effects of MMT addition with pyrolysis temperature (Table 2) that were related to this interfacial phenomenon. At 900°C, mechanical properties decreased with MMT addition from SiOC-900-Ar (E: 58 ± 1 GPa; H: 7.1 ± 0.2 GPa) to 2MMT-900-Ar (E: 52 ± 4 GPa; H: 6.4 ± 0.3 GPa); however, at 1200°C, MMT addition improved the mechanical properties between SiOC-1200-Ar (E: 71 ± 4 GPa; H: 8.0 ± 0.7 GPa) and 2MMT-1200-Ar (E: 81 ± 5 GPa; H: 8.3 ± 0.6 GPa). 2 wt% MMT again appeared to be the critical loading amount, below which 1MMT-900-Ar (E: 57 ± 4 GPa; H: 6.6 ± 0.7 GPa) and 1MMT-1200-Ar (E: 78 ± 3 GPa; H: 8.3 ± 0.5 GPa) foreshadowed the aforementioned trends observed at 900°C and 1200°C. Due to agglomeration effects, mechanical properties were indistinguishable between 2 wt% and 5 wt% MMT contents at both 900°C (E: 63 ± 1 GPa; H: 6.4 ± 0.2 GPa) and 1200°C (E: 58 ± 1 GPa; H: 7.1 ± 0.2 GPa).

The elimination of transient α-quartz and a completely formed amorphous SiOC matrix caused the improvement in Young's modulus between SiOC-900-Ar and SiOC-1200-Ar. At 900°C, increasing MMT content correlated with increasing concentrations of lingering interfacial Si-OH bonds; that is, as the MMT-SiOC interface was not fully formed, MMT domains were

View Article Online
DOI: 10.1039/D5TA03219A

effectively discontinuous inclusions and impeded the mechanical properties in 1/2/5MMT-900-Ar. When the interface was further refined at 1200°C, MMT strengthened the SiOC matrix even with H_2O injection due to inherent nanosheet anisotropy. Both E (53 ± 1 GPa) and H (5.9 ± 0.2 GPa) expectedly decreased in SiOC-1200-H_2O because of SiO_2 formation and C removal. MMT domains still abetted the mechanical strength in 2MMT-1200-H_2O (E: 59 ± 3 GPa; H: 6.4 ± 0.2 GPa), although the net reduction was caused by H_2O ingress into the SiOC matrix. Mechanical properties of *x*MMT-900-H_2O were not investigated in light of this interfacial evolution phenomenon and because the α-quartz content among MMT-900-Ar and MMT-900-H_2O appeared similar in XRD profiles. While MMT-SiOC interfacial refinement at 1200°C was assessed through trends among physical and mechanical properties, nanoscale ordering can only be ascertained through advanced TEM techniques (e.g., 4D-STEM) that require a separate study.

Carbothermal reduction at 1400°C accounted for the general decrease in CY and increase in VS (Figure 4(c)) through the formation of β-SiC phases and CO evolution in all MMT-SiOC ceramics across either pyrolysis atmosphere. Water vapor-assisted pyrolysis induced an additional ~2-4% mass loss in SiOC-1400-H_2O (CY: 71.1 ± 0.8%), 1/2MMT-1400-H_2O (CYs: ~72.2 ± 0.6%), and 5MMT-1400-H_2O (CY: 70.5 ± 0.4%) compared to SiOC-1400-Ar (CY: 73.2 ± 0.6%) and 1/2/5MMT-1400-Ar (CYs: ~74.5 ± 0.5%). The observed trends were attributed to accelerated CO evolution from β-SiC formation, as the XRD results (Figure 1(c)) revealed more prominent β-SiC reflections in 1/2/5MMT-1400-H_2O samples. While water vapor-assisted pyrolysis typically increases SiO_2 and decreases C contents, MMT domains and specifically MMT-SiOC interfaces appeared resistant to these effects. Anticipated bulk MMT effects such as nanosheet stacking and increased proximity of MMT regimes from high loading content manifested in a further 2% mass

View Article Online
DOI: 10.1039/D5TA03219A

loss in 5MMT-1400-H_2O. Analogous behavior was not appreciably observed in 5MMT-1400-Ar, presumably due to the abundance of free C.

Volumetric shrinkages among the Ar- and water vapor-pyrolyzed MMT-SiOC-1400 samples were generally identical within experimental error, with a slightly greater shrinkage observed in SiOC-1400-H_2O (VS: 49.0 ± 0.4%) and SiOC-1400-Ar (VS: 47.4 ± 0.5%) than in MMT-containing ceramics. Among MMT-SiOC-1400 ceramics, pyrolysis atmosphere had little effect on volumetric shrinkage at corresponding MMT content as shown between 1/2MMT-1400-H_2O (VSs: ~46.6 ± 0.7%) and 1/2MMT-1400-Ar (VSs: ~47.0 ± 0.5%), and between 5MMT-1400-H_2O (VS: 46.2 ± 0.4%) and 5MMT-1400-Ar (VS: 45.6 ± 0.7%). Above the stable temperature range of SiOC (from 1200-1300°C), *x*MMT-SiOC-1400 ceramics illustrated the thermal degradation behavior that would compromise MMT-SiOC microstructures, phase profiles, and physical properties.

Decreases in E and H among 1400°C ceramics were caused by intrinsic SiOC phase evolution, carbothermal processes (creating inherent porosity), and MMT decomposition. Compared to SiOC-1400-Ar (E: 56 ± 4 GPa; H: 6.0 ± 0.7 GPa), MMT decomposition and enhanced β-SiC nanowhisker growth contributed to net reductions observed with increasing MMT content from 1MMT-1400-Ar (E: 58 ± 5 GPa; H: 6.7 ± 0.7 GPa) to 2MMT-1400-Ar (E: 52 ± 4 GPa; H: 5.9 ± 0.7 GPa) and to 5MMT-1400-Ar (E: 52 ± 4 GPa; H: 6.2 ± 0.8 GPa). Strengthening mechanisms imbued by MMT domains at 1200°C with water vapor were absent in 2MMT-1400-H_2O (E: 51 ± 5 GPa; H: 5.8 ± 0.6 GPa), with a similar reduction compared to SiOC-1400-H_2O (E: 59 ± 5 GPa; H: 5.7 ± 0.6 GPa). MMT-SiOC mechanical properties across all pyrolysis temperatures resembled those of fused SiO_2 (E: ~70 GPa) when compared with β-SiC (E: ~400 GPa) or graphitic C (E: ~40 GPa (c-axis)), as strengthening effectively occurred by diffusion of

View Article Online
DOI: 10.1039/D5TA03219A

sp^3-C into the am-SiO_2/SiOC matrix.[27,42] The effect of MMT on mechanical properties was self-limited as MMT is intrinsically an oxide and interfacial α-quartz could weaken the ceramic nanocomposites with an excessively high loading content. Overall, while water vapor-assisted pyrolysis in pure SiOC affected physical and mechanical property changes through reduction of C and incorporation of O, MMT-SiOC ceramics did not show appreciable changes with increasing MMT content. That is, the incorporation of C into MMT domains produced net improvements in CY and VS among all MMT-SiOC-Ar ceramics. This phenomenon also occurred in MMT-SiOC-H_2O ceramics while C was removed in native SiOC-H_2O.

View Article Online
DOI: 10.1039/D5TA03219A

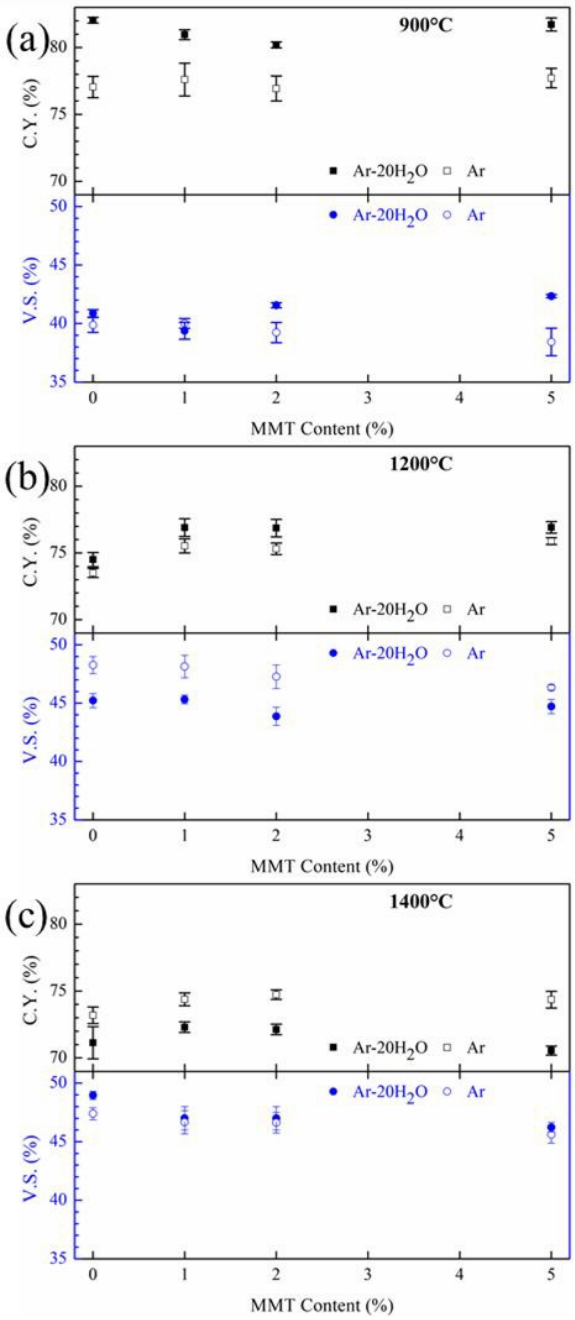

Figure 4. Ceramic yield (top panel/black) and volumetric shrinkage (bottom panel/blue) of MMT-SiOC ceramics pyrolyzed at (a) 900°C, (b) 1200°C, and (c) 1400°C in either Ar-20% H_2O (filled symbol) and Ar (unfilled). Error bars indicate a standard deviation of 3-5 samples.

View Article Online
DOI: 10.1039/D5TA03219A

Table 2. Elastic modulus (E/GPa) and hardness (H/GPa) values of MMT-SiOC ceramics pyrolyzed in Ar or Ar-20H_2O to 900, 1200, and 1400°C from nanoindentation. The error represented the standard deviation of 20-25 indents.

Ceramic Sample		E (GPa)			H (GPa)		
		900°C	1200°C	1400°C	900°C	1200°C	1400°C
Ar	SiOC	58 ± 1	71 ± 4	56 ± 4	7.1 ± 0.2	8.0 ± 0.7	6.0 ± 0.7
	1MMT	57 ± 3	78 ± 3	58 ± 5	6.6 ± 0.7	8.5 ± 0.5	6.7 ± 0.7
	2MMT	52 ± 4	81 ± 5	52 ± 4	5.9 ± 0.5	8.3 ± 0.6	5.9 ± 0.7
	5MMT	53 ± 1	77 ± 5	52 ± 5	6.4 ± 0.2	8.6 ± 0.7	6.2 ± 0.8
Ar-20H_2O	SiOC	---	53 ± 1	59 ± 5	---	5.9 ± 0.2	5.7 ± 0.6
	2MMT	---	59 ± 3	51 ± 5	---	6.4 ± 0.4	5.8 ± 0.6

3.3. Selectively-etched porosity for SiO_2 domain characterization

MMT-SiOC-H_2O ceramics showed a net reduction of crystallized α-quartz through XRD and TEM analysis, as water vapor produced sufficient •OH and •H radicals to vitrify crystalline Si-O-Si bonds. While water vapor produced a higher concentration of am-SiO_2, the total concentration and size of these nanosized SiO_2 domains were not apparent from the aforementioned analysis. To characterize SiO_2 content, porous ceramics were prepared by etching SiO_2 domains in MMT-SiOC-Ar and MMT-SiOC-H_2O with excess HF (Equation 8), and the effect of water vapor-assisted pyrolysis on selectively-etched porosity and SSAs in MMT-SiOC was determined with N_2 sorption experiments (Figure 5). In a previous study that mechanistically characterized the role of water vapor pyrolysis and HF etching in phase evolution and porosity, Si 2s (154 eV), Si 2p (103 eV), and O 1s (534 eV) XPS emission intensities were substantially reduced in conjunction with increasing intensity of the C 1s (285 eV) peak in SiOC regardless of Ar or Ar+H_2O pyrolysis.[3] This phenomenon corresponded to Si and O removal by HF and thus a higher concentration of C in HF-etched SiOC as C-C bonds were unaffected by HF. These effects

View Article Online
DOI: 10.1039/D5TA03219A

were also confirmed by elemental analysis: with Ar pyrolysis, the SiOC composition changed from 28.7 wt% Si to 18.3 wt% Si, 20.3 wt% O to 15.7 wt% O, and 51.1 wt% C to 66.0 wt% C with HF etching; for SiOC prepared with water vapor-assisted pyrolysis, Si and O removal was more apparent with larger decreases in Si and O amounts from 36.3 wt% to 18.1 wt% and from 36.7 wt% to 22.8 wt%, respectively.[3] In addition, XRD showed suppression of amorphous and crystalline SiO_2 reflections after HF etching, and HRTEM confirmed the evolution of 2-5 nm SiO_2 domains and pores before and after HF etching, respectively.[3]

$$SiO_2 + 6HF \rightarrow H_2SiF_6 + 2H_2O \quad (8)$$

Only 1200°C and 1400°C pyrolyzed and etched ceramics were reported in Figure 5 as XRD patterns, CY/VS trends, and nanoindentation results indicated that H_2 evolution and MMT-SiOC interface formation were not completed at 900°C. N_2 sorption data for HF-etched 900°C ceramics are provided in the Supplementary Information as these ceramics had a generally similar trend to HF-etched 1200°C ceramics. The SSAs of HF-etched MMT-SiOC were reported in Table 3. Selectively etched porosity was representative of the concentration, size, and distribution of SiO_2 domains present in the MMT-SiOC ceramics as Si-C and C-C bonds were resistant to HF.

MMT-SiOC pyrolyzed at 1200°C in Ar-20%H_2O exhibited a marked enhancement in pore volumes after HF etching, although porosity was primarily derived through the SiOC matrix. This was shown by marked increases in pore volumes between SiOC-1200-Ar (5 $cm^3 \cdot g^{-1}$) and SiOC-1200-H_2O (505 $cm^3 \cdot g^{-1}$). *x*MMT-1200-Ar were previously shown to marginally yet incrementally enhance pore volumes between 2 and 5 nm after HF etching with 2MMT-1200-Ar and 5MMT-1200-Ar exhibiting the best improvements with pore volumes of 25 $cm^3 \cdot g^{-1}$ and 30 $cm^3 \cdot g^{-1}$, respectively.[7] However, MMT addition contributed to smaller pore volumes in all water vapor-pyrolyzed and HF-etched 1MMT-1200-H_2O (150 $cm^3 \cdot g^{-1}$), 2MMT-1200-H_2O (165 $cm^3 \cdot g^{-1}$), and

View Article Online
DOI: 10.1039/D5TA03219A

5MMT-1200-H_2O (343 $cm^3 \cdot g^{-1}$), indicating that MMT did not promote or accelerate pore formation with water vapor-assisted pyrolysis. The reduction in porosity again contradicted the expected effect of water vapor to grow SiO_2 regimes.

Pore size distributions obtained from NLDFT fitting (Figure 5(c-d)) revealed a near-unimodal distribution of about 2 nm but less than 3 nm, reflecting the etched SiO_2 domains in SiOC-1200-H_2O. 1 wt% and 2 wt% MMT content decreased the concentration of these pores before increasing in 5 wt% MMT samples pyrolyzed at 1200°C, all without altering the intrinsic pore size distribution of SiOC-1200-H_2O. Therefore, the observed reduction in pore volume in *x*MMT-1200-H_2O was not related to SiO_2 growth/coalescence but rather a decrease in SiO_2 content in MMT-SiOC compared to SiOC. SSAs calculated from NLDFT fitting (Table 3) enumerated the decreased SiO_2 content in MMT-SiOC samples at 1200°C, with SSAs decreasing nearly 75% between SiOC-1200-H_2O (2081 $m^2 \cdot g^{-1}$) to 1MMT-1200-H_2O (656 $m^2 \cdot g^{-1}$). The two-fold increase between 2MMT-1200-H_2O (707 $m^2 \cdot g^{-1}$) and 5MMT-1200-H_2O (1441 $m^2 \cdot g^{-1}$) was associated with additional SiO_2 present in the latter (Figure 1(b)), presumably due to bulk effects from higher MMT content and excess evolved α-quartz at the MMT-SiOC interface that could not be incorporated within the amorphous SiOC matrix. Recalling that *x*MMT-1200-H_2O exhibited higher ceramic yields than *x*MMT-1200-Ar, the decrease in SiO_2 concentration was attributed to the retention of SiOC phases and oxidation resistance of MMT domains in water vapor-pyrolyzed MMT-SiOC.

Pore volumes (Figure 5(b)) and pore size distributions (Figure 5(d)) of HF-etched *x*MMT-1400-Ar and *x*MMT-1400-H_2O indicate the dissolution of distinct pore structures of the analogous 1200°C samples. SiOC-1400-H_2O (239 $cm^3 \cdot g^{-1}$), 1MMT-1400-H_2O (254 $cm^3 \cdot g^{-1}$), 2MMT-1400-H_2O (228 $cm^3 \cdot g^{-1}$), and 5MMT-1400-H_2O (218 $cm^3 \cdot g^{-1}$) all displayed identical pore characteristics.

View Article Online
DOI: 10.1039/D5TA03219A

Similarly observed in SiOC-1400-Ar and 1/2/5MMT-1400-Ar, the broadening of pore sizes between 2 and 5 nm illustrated the thermal degradation characteristics and the fate of the SiO_2 phase in MMT-SiOC upon pyrolysis above 1400°C. As a result, SSAs (Table 3) of SiOC-1400-H_2O (724 $m^2 \cdot g^{-1}$), 1MMT-1400-H_2O (757 $m^2 \cdot g^{-1}$), and 2MMT-1400-H_2O (657 $m^2 \cdot g^{-1}$) were generally identical, with a further reduction in SSA in 5MMT-1400-H_2O (498 $m^2 \cdot g^{-1}$) due to consumption of SiO_2 during carbothermal formation of β-SiC nanowhiskers. At all pyrolysis temperatures, MMT reduced the overall SiO_2 content in MMT-SiOC-H_2O ceramics compared to native SiOC, and the pore properties were primarily derived from the matrix SiOC, not from MMT regimes or the MMT-SiOC interface. Water vapor-assisted pyrolysis not only suppressed α-quartz evolution but also decreased the overall SiO_2 content in MMT-1200-H_2O. The latter surprisingly and severely contradicted typical microstructural evolution behavior in water vapor-assisted SiOC. While an oxide filler, nanostructured MMT did not impart additional SiO_2 domains compared to SiOC in the presence of water vapor, which contradicted the initial hypothesis of this study. Furthermore, the retention or incorporation of C was reinforced as the source of noted improvements in CY upon MMT addition.

View Article Online
DOI: 10.1039/D5TA03219A

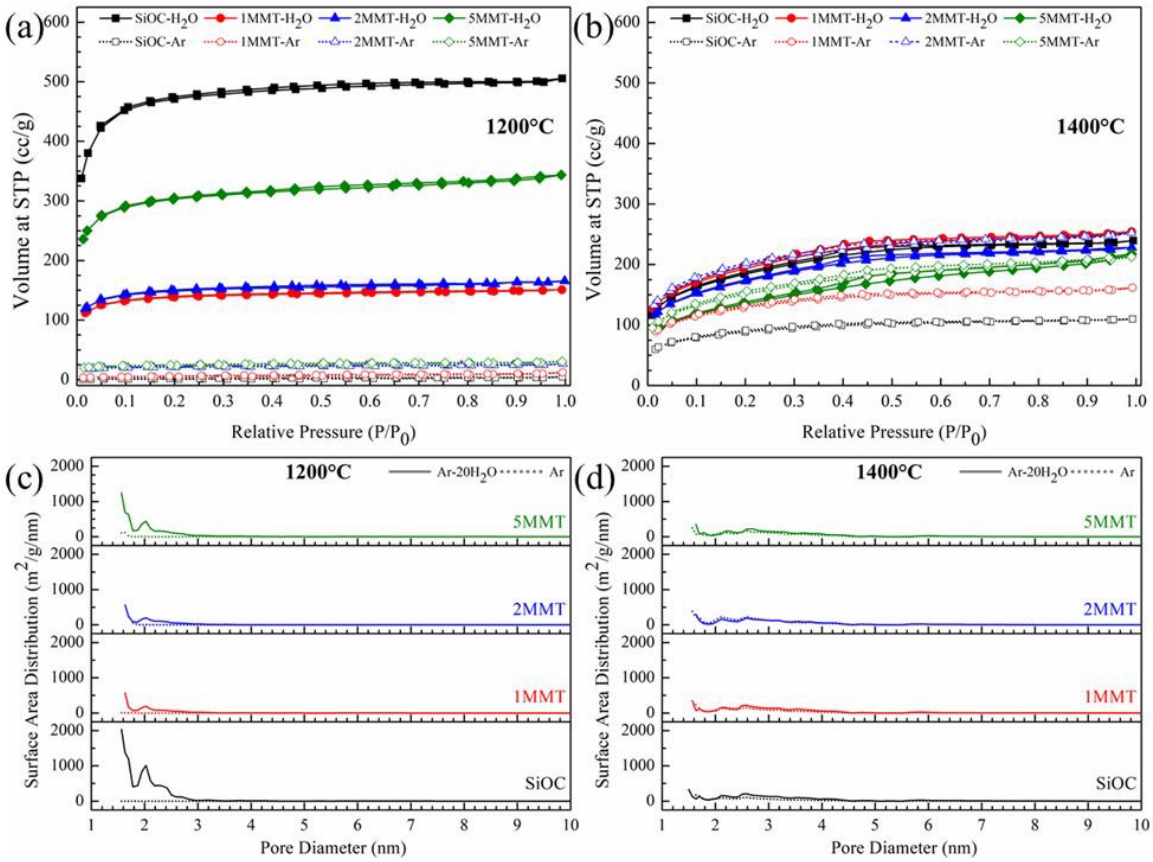

Figure 5. Porous structure characterization of HF-etched MMT-SiOC-Ar (dashed) and MMT-SiOC-H_2O (solid) with N_2 sorption. N_2 sorption isotherms of HF-etched *x*MMT-SiOC (*x* = 0/black, 1/red, 2/blue, 5/green) pyrolyzed at (a) 1200°C and (b) 1400°C. Pore size distributions of HF-etched *x*MMT-SiOC ceramics pyrolyzed at (c) 1200°C and (d) 1400°C as determined by NLDFT fitting. Pore size distributions were offset for clarity.

Table 3. Calculated SSAs of etched *x*MMT-SiOC-Ar and *x*MMT-SiOC-H_2O ceramics. SSAs were determined by NLDFT fitting of adsorption branches using a silica adsorbate model with spherical/cylindrical pore structures.

View Article Online
DOI: 10.1039/D5TA03219A

Ceramic Sample	Specific Surface Area ($m^2 \cdot g^{-1}$)			
	1200°C		1400°C	
	Ar	Ar-H_2O	Ar	Ar-H_2O
SiOC	3	2081	340	724
1MMT	20	656	499	757
2MMT	105	707	772	657
5MMT	120	1441	574	498

3.4. Compositional analysis and mechanistic understanding

Water vapor-assisted pyrolysis clearly did not enhance SiO_2 formation in MMT-SiOC, so compositional analysis was performed on SiOC-1200-Ar, SiOC-1200-H_2O, 2MMT-1200-Ar, and 2MMT-1200-H_2O to understand the distribution of SiO_xC_y and C phases. The concentration of amorphous SiO_xC_y (I – SiO_2, II – $SiO_{1.5}C_{0.25}$, III – $SiOC_{0.5}$, IV – $SiO_{0.5}C_{0.75}$, V – SiC) phases was quantitatively analyzed with ^{29}Si NMR as the unique chemical environments about each Si nucleus may be differentiated. Figure 6(a) depicts the ^{29}Si NMR spectra of SiOC-1200-Ar (black dotted), SiOC-1200-H_2O (black solid), 2MMT1-1200-Ar (blue dotted), and 2MMT-1200-H_2O (blue solid) with the expected chemical shifts and Si tetrahedral structures of SiO_2 (-108 ppm), $SiO_{1.5}C_{0.25}$ (-68 ppm), $SiOC_{0.5}$ (-34 ppm), $SiO_{0.5}C_{0.75}$ (10 ppm), and SiC (-11 ppm) sourced from literature and indicated.[36,43,44] A small overtone peak (I') at ~ -125 ppm causing peak asymmetry of peak I (SiO_2) was attributed to non-structural 5-coordinated SiO_4 from interactions with neighboring O atoms; while the authors could not find an appropriate reference for this peak in SiOC systems, a similar effect was observed in amorphous Si_3N_4 systems and the rationale was applied to this system.[45] This I' peak was not included in composition and phase fraction calculations because it did not represent a unique Si bonding environment – see the Supplementary Information for details.

SiOC-1200-Ar was revealed to contain SiO_2, $SiO_{1.5}C_{0.25}$, $SiOC_{0.5}$, and SiC units that converted to predominantly SiO_2 upon water vapor-assisted pyrolysis in SiOC-1200-H_2O.

View Article Online
DOI: 10.1039/D5TA03219A

Notably, 2MMT-1200-Ar showed the emergence of $SiO_{0.5}C_{0.75}$ clusters between 50 and 20 ppm, which were not present in SiOC systems and have seldom been reported. MMT generally provides characteristic peaks between -90 and -110 ppm as shown in previous ^{29}Si NMR characterization studies,[46-48] so the new Si bonding environment in 2MMT-1200-Ar was not from MMT itself but from $SiO_{0.5}C_{0.75}$ clusters presumably at the MMT-SiOC interface. Similar to SiOC-1200-H_2O, water vapor-assisted pyrolysis induced restructuring of Si tetrahedra in 2MMT-1200-H_2O to predominantly SiO_2; however, some $SiO_{0.5}C_{0.75}$ and SiC clusters were retained. While SiO_2 clusters in SiOC-1200-H_2O were completely removed with water vapor-assisted pyrolysis, some SiO_2 in 2MMT-1200-H_2O was oxidation resistant to water vapor ingress between 500°C and 700°C, indicating that these clusters may have formed during the early stages of the polymer-to-ceramic transformation (300°C to 500°C).

Gaussian peak deconvolution (Figure 6(b)) further quantified these trends as the integrated area of each peak provided the relative phase fractions of SiO_xC_y phases and the calculated NMR composition of the SiOC matrix. Full Gaussian peak fitting details may be found in the Supplemental Information. Matrix compositions for SiOC-1200-Ar ($SiO_{1.06}C_{0.47}$) and 2MMT-1200-Ar ($SiO_{1.10}C_{0.45}$) were nearly identical but were comprised of unique distributions of SiO_xC_y phases. MMT addition primarily induced restructuring of $SiO_{1.5}C_{0.25}$ (11.4% in SiOC-1200-Ar to 6.4% in 2MMT-1200-Ar), $SiOC_{0.5}$ (13.8% to 4.7%), SiC (32.1% to 13.3%), and $SiO_{0.5}C_{0.75}$ (~0% to 36.5%). The slight increase in SiO_2 content (37.6% to 39.2%) upon MMT addition was attributed to interfacial α-quartz and MMT itself. It was postulated that $SiO_{0.5}C_{0.75}$ existed at or near the MMT-SiOC interface, which bridged between crystalline MMT and amorphous SiOC. Furthermore, the higher concentration of retained free C around the MMT domains contributed to the accelerated β-SiC formation observed in the MMT-SiOC ceramics at 1400°C (Figure 3(c)).

View Article Online
DOI: 10.1039/D5TA03219A

This would further indicate that MMT was thoroughly incorporated and embedded in the SiOC matrix at the nanoscale as additional SiO_xC_y phases were formed to resolve the incoherency at the interface.

While water vapor-assisted pyrolysis significantly altered the matrix composition ($SiO_{1.93}C_{0.04}$) in SiOC-1200-H_2O to mainly SiO_2 (88.4%) with small amounts of $SiO_{1.5}C_{0.25}$ (7.3%) and $SiOC_{0.5}$ (4.2%), 2MMT-1200-H_2O ($SiO_{1.50}C_{0.25}$) was partially resistant to water vapor attack between 500°C to 700°C as SiC (8.3%) and $SiO_{0.5}C_{.75}$ (17.9%) were retained in appreciable amounts and less SiO_2 (62.3%) was formed. This finding supported the observed decrease in pore volumes and SSAs in *x*MMT-900-H_2O and *x*MMT-1200-H_2O ceramics after HF etching compared to SiOC-900-H_2O and SiOC-1200-H_2O (Figure 5). The retained yet decreased SiC and $SiO_{0.5}C_{0.75}$ contents indicated that the domains around MMT or the MMT-SiOC interface were oxidation-resistant, but the size of the MMT-SiOC interface may have decreased upon water vapor pyrolysis. As the SiOC matrix is inherently SiO_2-rich as evidenced by STEM-EDS elemental ratios (Table 2) after water vapor pyrolysis, fewer SiO_xC_y clusters were necessary to bridge the coherency gap between crystalline MMT and amorphous SiOC, or am-SiO_2 in the case of SiOC-1200-H_2O. The MMT-SiOC interfacial zones effectively decreased in size with Ar+H_2O. However, advanced nanoscale characterization such as synchrotron X-ray or 4D-STEM would be needed to discern changes in crystallinity and amorphous ordering across the MMT-SiOC interface.

As a carbon-rich SiO_xC_y phase, $SiO_{0.5}C_{0.75}$ clusters revealed in ^{29}Si NMR suggested higher C retention in MMT-SiOC at or near the interface. The nature of C in MMT-SiOC was characterized by Raman spectroscopy (Figure 6(c)) and elemental analysis (Table 4) to ascertain the effect of MMT on C content and structure. Raman analysis revealed no significant differences in C ordering among SiOC-1200-Ar, SiOC-1200-H_2O, 2MMT-1200-Ar, and 2MMT-1200-H_2O as

View Article Online
DOI: 10.1039/D5TA03219A

C appeared to be comparably disordered as evidenced by the D band at ~1330 cm^{-1}. The apparent G band at ~1600 cm^{-1} was determined to have contributions from the actual G band (~1550 cm^{-1}) and an overtone D' band (~1620 cm^{-1}), the presence of the latter was confirmed by D+D' (~2950 cm^{-1}) and 2D' (~3200 cm^{-1}) bands. Superposition of D' and G bands was commonly reported in disordered carbons, but the difference between the apparent G (G_{app}) and the inferred D' (D'_{inf}) bands from the 2D' band was shown to provide more information about the state of C with respect to graphene, graphene oxide (GO), or reduced graphene oxide (rGO).[49,50] Graphene was characterized by a ($D'_{inf} - G_{app}$) difference greater than 25, rGO by a difference between 0 and 25, and GO by a difference less than 0.[49] In all samples, 2D' was determined to be ~3180-3190 cm^{-1}, yielding D'_{inf} of ~1590-1595 cm^{-1}, and G_{app} was ~1605 cm^{-1}, indicating that C regimes existed primarily as GO phases with a high degree of disorder. Furthermore, a D+D" overtone band at ~2450 cm^{-1} revealed a D" band at ~1180 cm^{-1}, originating from sp^2-sp^3 interactions.

Lorentzian peak deconvolution of D and G_{app} (Figure 6(d)) further confirmed the similarity of C regimes among the four ceramic samples with A_D/A_G ratios of 5.45, 5.59, 4.49, and 5.86 for SiOC-1200-Ar, SiOC-1200-H_2O, 2MMT-1200-Ar, and 2MMT-1200-H_2O, respectively. Full Lorentzian peak deconvolution and Raman peak information can be found in the Supplemental Information. Due to the significant overlap of D, D', and G bands, the typical I_D/I_G ratio to determine the degree of disorder was not valid for such disordered carbons, so the integrated area ratio A_D/A_G was chosen to better quantify D and G contributions.[51,52] The Tuinstra-Koenig equation (Equation 9) relating lateral crystalline size (L_α) to A_D/A_G, with λ the laser excitation wavelength (532 nm), yielded similar L_α values of 3.3, 3.2, 3.9, and 3.1 nm, respectively. The marginal increase in crystallite size at 2MMT-1200-Ar was not deemed significant. Overall, neither water vapor-assisted pyrolysis nor MMT addition altered C structuring in MMT-SiOC.

View Article Online
DOI: 10.1039/D5TA03219A

$$L_\alpha = (2.4 * 10^{-10})\lambda^4 \left(\frac{A_D}{A_G}\right)^{-1} \quad (9)$$

Elemental analysis (E.A.) was performed to determine the total Si and C content in SiOC-1200-Ar, SiOC-1200-H_2O, 2MMT-1200-Ar, and 2MMT-1200-H_2O. O was determined as the residual from 100%. Some Si loss was observed during water vapor-assisted pyrolysis between SiOC-1200-Ar (28.5 wt%) and SiOC-1200-H_2O (26.3 wt%), as well as between 2MMT-1200-Ar (27.8 wt%) and 2MMT-1200-H_2O (26.3 wt%). While this was attributed to a small amount of Si evolution during water vapor injection, the overall Si content was generally invariant. Agreeing with previous studies,[3,15,16] water vapor pyrolysis aggressively removed C between SiOC-1200-Ar (31.7 wt%) and SiOC-1200-H_2O (20.6 wt%) through oxidation of free C. However, not only did MMT addition increase the C content by 15 wt% in 2MMT-1200-Ar (46.6 wt%), but also MMT addition proved to show resistance to water vapor ingress as the C content in 2MMT-1200-H_2O (43.9 wt%) did not decrease similarly to that in SiOC-1200-H_2O.

From the overall (E.A.) composition calculated from Si, O, and C content (Table 4) and the matrix composition calculated from ^{29}Si NMR (Figure 6(c) and also provided in Table 4), the stochiometric SiO_xC_y and free C phase compositions were described as $SiO_xC_y + zC_{free}$. In each sample, the O coefficient from E.A. was higher than the matrix O content from ^{29}Si NMR, so the excess O was assigned to the free C phase in the form of GO following Raman analysis. While the relative free C to SiO_xC_y ratio in SiOC-1200-Ar ($Si\ O_{1.06}\ C_{0.47}$ + 2.1 $CO_{0.65}$) did not appreciably decrease in SiOC-1200-H_2O ($SiO_{1.93}C_{0.04}$ + 1.8 $CO_{0.90}$), the free C phase was more oxidized, as was expected from prior studies. Not only did the free C phase content increase with MMT addition for both 2MMT-1200-Ar ($SiO_{1.10}C_{0.45}$ + 3.5 $CO_{0.15}$) and 2MMT-1200-H_2O ($SiO_{1.50}C_{0.25}$ + 3.7 $CO_{0.13}$), but also the phase was less oxidized. Overall, while MMT addition did not alter the size or bonding characteristics of the free C phase, it encapsulated more C within the MMT-SiOC

View Article Online
DOI: 10.1039/D5TA03219A

interface that was resistant to water vapor oxidation during the polymer-to-ceramic transformation. Even if potentially further oxidized, C was preferentially retained in the MMT-SiOC matrix as GO and not evolved as CO.

Figure 7 summarizes phase evolution mechanisms in MMT-SiOC-Ar and MMT-SiOC-H_2O ceramics from the preceramic MMT-PSO through stages before and after water vapor injection between 500°C and 1200°C. During phase evolution in the polymer-to-ceramic transformation, MMT regimes retained more C from the preceramic polymer within the interfacial region between 400°C and 500°C when silane condensation reactions occurred earlier with MMT addition, as shown by TGA.[7,35] In these regions of nascent SiOC, the matrix retained more C around MMT regimes acting as a SiO_2 source to maintain the overall matrix composition of the MMT-SiOC ceramics, which were shown earlier by ^{29}Si NMR to be identical between SiOC-1200-Ar and 2MMT-1200-Ar. As this event occurred prior to water vapor injection in the 2MMT-SiOC samples, nascent SiOC regimes about MMT were not as susceptible to oxidation as similar phases forming in SiOC around 475-500°C.[7] While producing SiO_2 structures and removing C in pure SiOC matrix, water vapor-assisted pyrolysis preferentially incorporated and retained C within amorphized α-quartz domains. In MMT-SiOC-Ar, α-quartz exists solely within the MMT interfacial region with a small concentration of SiO_2 clusters forming in the matrix. In the presence of H_2O, there is a higher concentration of am-SiO_2 in the SiOC matrix but α-quartz is transformed to am-SiO_2 with more C retained within the MMT-SiOC interface.

In SiOC systems, free C is modeled as surrounding and diffusing into SiO_2 clusters to form SiO_xC_y tetrahedra.[22] The emergence of the $SiO_{0.5}C_{0.75}$ phase in 2MMT-1200-Ar supported this mechanistic explanation. In MMT-SiOC, additional C was retained to resolve structural incoherency between crystalline MMT and amorphous SiOC. Coherency and interfacial bonding

View Article Online
DOI: 10.1039/D5TA03219A

occurred through $SiO_{0.5}C_{0.75}$, SiC, and $SiOC_{0.5}$ phases, which formed through C diffusion into encapsulated regimes. Forming earlier in MMT-SiOC than in pure SiOC, these regimes were resistant to water vapor attack. The effects of water vapor on phase formation, composition, and selectively etched porosity were then only a function of the SiOC matrix with MMT decreasing the total SiO_2 content.

The presence of MMT appreciably altered the effects of Ar+H_2O pyrolysis, in which SiO_2 suppression and C retention starkly contradicted expected results from previous studies. Water vapor-assisted pyrolysis further elucidated that the MMT-SiOC interface was active in radical-mediated reactions during the polymer-to-ceramic transformation, essentially classifying 2D nanostructured MMT as a hybrid active-passive filler for PDCs. The findings of this study further MMT's potential as a sustainable, naturally derived reinforcement in high-temperature ceramic composites through a fundamental understanding of MMT's contribution to phase evolution and material properties in the MMT-SiOC system. In particular, this methodology could be transferred to other 2D ceramic nanocomposite systems: for example, $Ti_3C_2T_x$ (MXene)-SiOC nanocomposites, which are attractive candidate materials for electrically-conductive yet thermally-insulating applications, prepared in a similar manner, were also characterized with interfacial α-quartz.[53,54] whose suppression can expand the viable temperature range above ~600°C as potential fracture from the α-to-β transformation was mitigated.

View Article Online
DOI: 10.1039/D5TA03219A

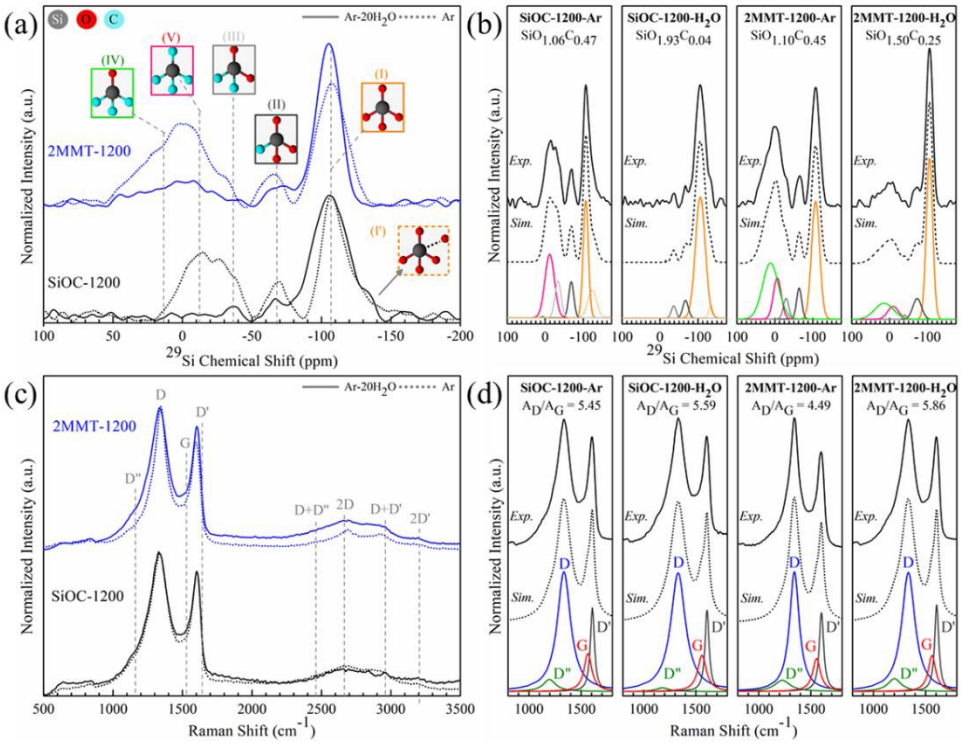

Figure 6. (a) ^{29}Si NMR spectra of SiOC-1200-Ar (black/dotted), SiOC-1200-H_2O (black/solid), 2MMT-1200-Ar (blue/dotted), and 2MMT-1200-H_2O (blue/solid). Peaks I-V indicate the chemical shifts and Si tetrahedral structure of SiO_2 (-108 ppm/orange), $SiO_{1.5}C_{0.25}$ (-68 ppm/dark grey), $SiOC_{0.5}$ (-34 ppm/light gray), $SiO_{0.5}C_{0.75}$ (10 ppm/green), and SiC (-11 ppm/pink), respectively; (b) deconvoluted and simulated ^{29}Si NMR spectra with calculated compositions. Full peak fitting details are provided in the Supplemental Information; (c) Raman spectra of SiOC-1200-Ar (black/dotted), SiOC-1200-H_2O (black/solid), 2MMT-1200-Ar (blue/dotted), and 2MMT-1200-H_2O (blue/solid); (d) D/G peak deconvolution (D: blue; G: red; D': gray; D": green) and calculated A_D/A_G ratio for previous samples. Peak fitting details are provided in the Supplemental Information.

Table 4. Elemental analysis (E.A.), NMR, and calculated $SiO_xC_y + zC_{free}$ compositions of SiOC-1200-Ar, SiOC-1200-H_2O, 2MMT-1200-Ar, and 2MMT-1200-H_2O. As the NMR composition

View Article Online
DOI: 10.1039/D5TA03219A

only considered C and O bonded to Si, the free C phase content and composition were extracted from the E.A. composition.

Sample	Elemental Analysis (E.A.)			E.A. Composition	NMR Composition	$SiO_xC_y + zC_{free}$
	Si (wt%)	O (wt%)	C (wt%)			
SiOC-1200-Ar	28.5	39.8	31.7	$Si\ O_{2.45}\ C_{2.59}$	$Si\ O_{1.06}\ C_{0.47}$	$Si\ O_{1.06}\ C_{0.47} + 2.1\ CO_{0.65}$
SiOC-1200-H_2O	26.3	53.2	20.6	$Si\ O_{3.54}\ C_{1.83}$	$Si\ O_{1.93}\ C_{0.04}$	$Si\ O_{1.93}\ C_{0.04} + 1.8\ CO_{0.90}$
2MMT-1200-Ar	27.8	25.7	46.6	$Si\ O_{1.62}\ C_{3.92}$	$Si\ O_{1.10}\ C_{0.45}$	$Si\ O_{1.10}\ C_{0.45} + 3.5\ CO_{0.15}$
2MMT-1200-H_2O	26.3	29.8	43.9	$Si\ O_{1.98}\ C_{3.90}$	$Si\ O_{1.50}\ C_{0.25}$	$Si\ O_{1.50}\ C_{0.25} + 3.7\ CO_{0.13}$

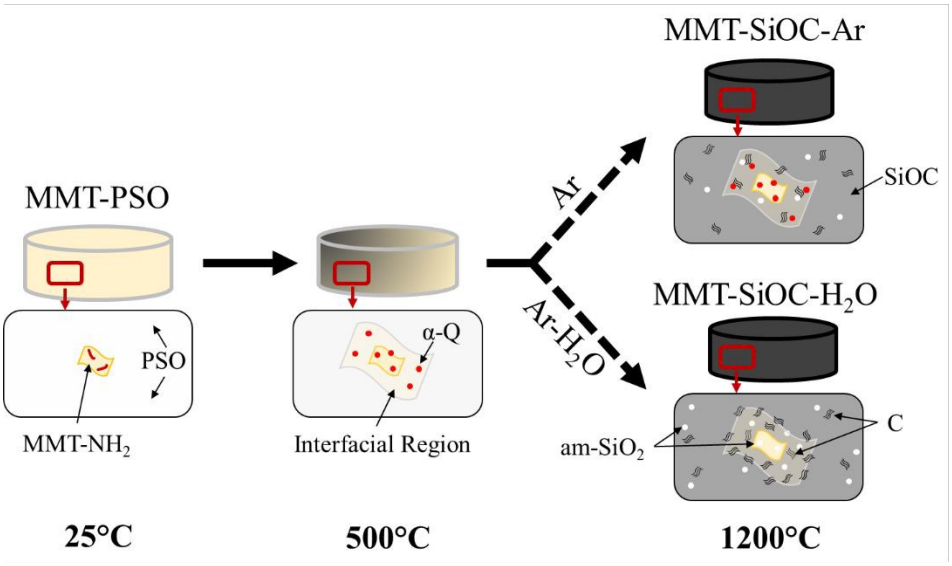

Figure 7. Schematic of phase evolution mechanisms in MMT-SiOC-Ar and MMT-SiOC-H_2O ceramics. With water vapor-assisted pyrolysis, α-quartz (α-Q) converted to am-SiO_2, and more free C was retained within the MMT-SiOC interfacial regime.

4. Conclusions

In this study, MMT-SiOC-Ar and MMT-SiOC-H_2O nanocomposites were prepared to mechanistically determine the effect of water vapor on SiO_2 phase evolution and material properties. Water vapor-assisted pyrolysis typically removes free C and drastically increases amorphous SiO_2 clusters between 2 nm and 5 nm in pure SiOC. MMT domains not only inhibited

View Article Online
DOI: 10.1039/D5TA03219A

H_2O ingress to reduce SiO_2 content compared to native SiOC (as shown by N_2 sorption experiments) but also selectively amorphized crystalline α-quartz and encapsulated/shielded C from volatilization (as confirmed by (HR)TEM analysis). H_2O injection activated and vitrified Si-O-Si bonds, which then reacted with hydrocarbon gases during pyrolysis to retain C. ^{29}Si NMR characterization revealed the emergence of $SiO_{0.5}C_{0.75}$ clusters in MMT-SiOC that were postulated to form within the MMT-SiOC interface and were retained after Ar-H_2O pyrolysis. Encapsulated SiOC/C regimes further contributed to enhanced β-SiC nanowhisker growth as shown by SEM and XRD. This study challenged conventional assumptions about reactive pyrolysis in PDCs through new findings of encapsulation, shielding, and retention of C as graphene oxide in MMT-SiOC-H_2O ceramics under the simultaneous presence of MMT and water vapor and a mechanistic understanding of interfacial phenomena and phase formation in MMT-SiOC ceramic nanocomposites. It opens new avenues for tailoring nanocomposite interfaces in designing multifunctional or porous ceramics with targeted phase compositions and using natural nanostructured additives to achieve high-performance materials through sustainable methods.

5. End of Document Items

5.1. CRediT Authorship Contribution Statement:

Advaith V. Rau: Conceptualization, Methodology, Validation, Formal analysis, Investigation, Resources, Data curation, Writing – Original Draft, Writing – Review & Editing, Supervision, Visualization. **Kathy Lu:** Resources, Writing – Review & Editing, Supervision, Project administration, Funding acquisition.

View Article Online
DOI: 10.1039/D5TA03219A

5.2. Declaration of Competing Interest:

The authors declare that they have no known competing financial interests or personal relationships that could have appeared to influence the work reported in this paper.

5.3. Funding:

This work was supported by the National Science Foundation under grant number CBET-2024546 and the Air Force Office of Scientific Research under grant numbers FA9550-22-1-0081 and FA9550-24-1-0301.

5.4. Acknowledgement:

This work was made possible by the use of Virginia Tech's Materials Characterization Facility, which is supported by the Institute for Critical Technology and Applied Science, the Macromolecules Innovation Institute, and the Office of the Vice President for Research and Innovation.

5.5. Data availability

The raw and processed data required to reproduce these findings are available upon request.

6. References:

1. K. Lu, *Materials Science and Engineering: R: Reports*, 2015, **97**, 23-49.
2. K. Lu and D. Erb, *International Materials Reviews*, 2017, **63**, 139-161.
3. K. Lu and J. Li, *Journal of the European Ceramic Society*, 2016, **36**, 411-422.
4. D. Erb and K. Lu, *Journal of the American Ceramic Society*, 2018, **101**, 5378-5388.
5. T. Chen, Y. Yuan, Y. Zhao, F. Rao and S. Song, *Langmuir*, 2019, **35**, 2368-2374.
6. E. Bernardo, P. Colombo and E. Manias, *Ceramics International*, 2006, **32**, 679-686.
7. A. V. Rau and K. Lu, *Small*, 2025, **21,** 2408218.

View Article Online
DOI: 10.1039/D5TA03219A

8. T. Liang, Y.-L. Li, D. Su and H.-B. Du, *Journal of the European Ceramic Society*, 2010, **30**, 2677-2682.
9. G. S. Bibbo, P. M. Benson and C. G. Pantano, *Journal of Materials Science*, 1991, **26**, 5075-5080.
10. P. Colombo, T. E. Paulson and C. G. Pantano, *Journal of Sol-Gel Science and Technology*, 1994, **2**, 601-604.
11. H. Ding and M. J. Demkowicz, *Sci Rep*, 2015, **5**, 13051.
12. M. Narisawa, H. Hokazono, K. Mitsuhara, H. Inoue and T. Ohta, *Journal of the Ceramic Society of Japan*, 2016, **124**, 1094-1099.
13. G. D. Sorarù, C. Tavonatti, L. Kundanati, N. Pugno and M. Biesuz, *Journal of the American Ceramic Society*, 2020, **103**, 6519-6530.
14. A. H. Tavakoli, M. M. Armentrout, M. Narisawa, S. Sen, A. Navrotsky and R. Riedel, *Journal of the American Ceramic Society*, 2015, **98**, 242-246.
15. J. Li, K. Lu, *Journal of the American Ceramic Society*, 2015, **98**, 2357-2365.
16. K. Bawane, D. Erb and K. Lu, *Journal of the European Ceramic Society*, 2019, **39**, 2846-2854.
17. N. Yang, M. Gao, J. Li and K. Lu, *Journal of the American Ceramic Society*, 2019, **103**, 145-157.
18. E. Ionescu, C. Terzioglu, C. Linck, J. Kaspar, A. Navrotsky, R. Riedel and L. Gauckler, *Journal of the American Ceramic Society*, 2013, **96**, 1899-1903.
19. M. Narisawa, K. Yamada, U. Sakura and H. Inoue, *Journal of the American Ceramic Society*, 2019, **102**, 6449-6454.
20. H. Chaney and K. Lu, *Ceramics International*, 2023, **49**, 10193-10197.
21. K. Lu and H. Chaney, *Journal of the American Ceramic Society*, 2023, **106**, 2737-2743.

View Article Online
DOI: 10.1039/D5TA03219A

22. A. Saha and R. Raj, *Journal of the American Ceramic Society*, 2007, **90**, 578-583.

23. P. V. López, A. Mocciaro, M. F. Hernández, D. Richard and N. M. Rendtorff, *International Journal of Applied Ceramic Technology*, 2024, **21**, 4081-4090.

24. A. M., K. S. H. and N. S. M., *The International Conference on Applied Mechanics and Mechanical Engineering*, 2008, **13**, 37-49.

25. M. Romero, I. Padilla, M. Contreras and A. López-Delgado, *Minerals*, 2021, **11**, 332.

26. M. Wang, L. Li, Z. Li, M. Du, J. Liu, Q. Zhou and Z. Feng, *Ceramics International*, 2019, **45**, 11131-11135.

27. *Springer Handbook of Glass*, Springer Cham, 1 edn., 2019.

28. G. V. Gibbs, D. F. Cox, M. B. Boisen, R. T. Downs and N. L. Ross, *Physics and Chemistry of Minerals*, 2003, **30**, 305-316.

29. R. M. Hazen, L. W. Finger, R. J. Hemley and H. K. Mao, *Solid State Communications*, 1989, **72**, 507-511.

30. Y. Nakamura, J. Muto, H. Nagahama, I. Shimizu, T. Miura and I. Arakawa, *Geophysical Research Letters*, 2012, **39**, L21303.

31. V. Proust, M. C. Bechelany, R. Ghisleni, M.-F. Beaufort, P. Miele and S. Bernard, *Journal of the European Ceramic Society*, 2016, **36**, 3671-3679.

32. R. Sreeja, B. Swaminathan, A. Painuly, T. V. Sebastian and S. Packirisamy, *Materials Science and Engineering B*, 2010, **168**, 204-207.

33. J. L. Plawsky, F. Wang and W. N. Gill, *AIChE Journal*, 2002, **48**, 2315-2323.

34. C. Garcia-Garrido, P. E. Sanchez-Jimenez, L. A. Perez-Maqueda, A. Perejon and J. M. Criado, *Phys Chem Chem Phys*, 2016, **18**, 29348-29360.

35. A. V. Rau, K. Knott and K. Lu, *Materials Chemistry Frontiers*, 2021, **5**, 6530-6545.

View Article Online
DOI: 10.1039/D5TA03219A

36. B. Du, J. Qian, P. Hu, C. He, M. Cai, X. Wang and A. Shui, *Journal of the American Ceramic Society*, 2019, **103**, 1732-1743.

37. Y. Gao, Y. Bando, T. Sato and Y. Kitami, *Jpn. J. Appl. Phys*, 2001, **40**, 1065-1067.

38. Y. Gou, X. Tong, Q. Zhang, B. Wang, Q. Shi, H. Wang, Z. Xie and Y. Wang, *Ceramics International*, 2016, **42**, 681-689.

39. Z. Yu, L. Yang, H. Min, P. Zhang, C. Zhou and R. Riedel, *J. Mater. Chem. C*, 2014, **2**, 1057-1067.

40. M. Hojamberdiev, R. M. Prasad, C. Fasel, R. Riedel and E. Ionescu, *Journal of the European Ceramic Society*, 2013, **33**, 2465-2472.

41. A. Jain, S. P. Ong, G. Hautier, W. Chen, W. D. Richards, S. Dacek, S. Cholia, D. Gunter, D. Skinner, G. Ceder and K. A. Persson, *APL Materials*, 2013, **1**, 011002.

42. C. Stabler, E. Ionescu, M. Graczyk-Zajac, I. Gonzalo-Juan and R. Riedel, *Journal of the American Ceramic Society*, 2018, **101**, 4817-4856.

43. I. Hung, E. Ionescu, J. Sen, Z. Gan and S. Sen, *The Journal of Physical Chemistry C*, 2021, **125**, 4777-4784.

44. G. Mera, A. Navrotsky, S. Sen, H.-J. Kleebe and R. Riedel, *J Mater Chem A*, 2013, **1**.

45. I. Ponomarev and P. Kroll, *Materials (Basel)*, 2018, **11**, 1646.

46. I. W. M. Brown, K. J. D. MacKenzie and R. H. Meinhold, *Journal of Materials Science*, 1987, **22**, 3265-3275.

47. J. Grandjean, J. Bujdák and P. Komadel, *Clay Minerals*, 2018, **38**, 367-373.

48. A. K. Mishra, S. Allauddin, R. Narayan, T. M. Aminabhavi and K. V. S. N. Raju, *Ceramics International*, 2012, **38**, 929-934.

View Article Online
DOI: 10.1039/D5TA03219A

49. A. A. King, B. R. Davies, N. Noorbehesht, P. Newman, T. L. Church, A. T. Harris, J. M. Razal and A. I. Minett, *Sci Rep*, 2016, **6**, 19491.

50. Z. Li, L. Deng, I. A. Kinloch and R. J. Young, *Progress in Materials Science*, 2023, **135**, 101089.

51. M. G. d. S. Luiz Gustavo Cançado, F. H. Erlon H Martins Ferreira, Katerina Kampioti, Kai Huang, Alain Pénicaud, Carlos Alberto Achete, Rodrigo B Capaz and A. Jorio, *2D Materials*, 2017, **4**, 025039.

52. N. Yang and K. Lu, *Carbon*, 2021, **171**, 88-95.

53. A. V. Rau and K. Lu, *in review*, 2025.

54. A. V. Rau and K. Lu, *Advanced Composites and Hybrid Materials*, 2025, **8**, 253.

View Article Online
DOI: 10.1039/D5TA03219A

Data Availability Statement

Data will be made available upon request.